A NUMERICAL ANALYSIS OF INTERDIGITATED BACK CONTACTED SILICON SOLAR CELLS

A THESIS SUBMITTED TO
THE GRADUATE SCHOOL OF NATURAL AND APPLIED SCIENCES
OF
MIDDLE EAST TECHNICAL UNIVERSITY

BY

BERAN ACAR

IN PARTIAL FULFILLMENT OF THE REQUIREMENTS
FOR
THE DEGREE OF MASTER OF SCİENCE
IN
ELECTRICAL AND ELECTRONICS ENGINEERING

JANUARY 2018

Approval of the Thesis:

A NUMERICAL ANALYSIS OF INTERDIGITATED BACK CONTACTED SILICON SOLAR CELLS

Submitted by **BERAN ACAR** in partial fulfillment of the requirements for the degree of **Master of Science in Electrical and Electronics Engineering Department, Middle East Technical University** by,

Prof. Dr. Gülbin Dural Ünver _____
Dean, Graduate School of **Natural and Applied Sciences**

Prof. Dr. Tolga Çiloğlu _____
Head of Department, **Electrical and Electronics Engineering**

Yrd. Doç. Selçuk Yerci _____
Supervisor, **Electrical and Electronics Engineering Dep., METU**

Prof. Dr. Raşit Turan _____
Co-Supervisor, **Physics Dep., METU**

Examining Committee Members:

Doç. Dr. Barış Bayram _____
Electrical and Electronics Engineering Dep., METU

Yrd. Doç. Selçuk Yerci _____
Electrical and Electronics Engineering Dep., METU

Yrd. Doç. Serdar Kocaman _____
Electrical and Electronics Engineering Dep., METU

Prof. Dr. Atilla Aydınlı _____
Electrical and Electronics Engineering Dep., Uludağ University

Doç. Dr. Tuğba Selcen Navruz _____
Electrical and Electronics Engineering Dep., Gazi University

Date: *19.01.2018*

I hereby declare that all information in this document has been obtained and presented in accordance with academic rules and ethical conduct. I also declare that, as required by these rules and conduct, I have fully cited and referenced all material and results that are not original to this work.

Name, Lastname: Beran ACAR

Signature:

ABSTRACT

A NUMERICAL ANALYSIS OF INTERDIGITATED BACK CONTACTED SILICON SOLAR CELLS

ACAR, Beran

M.S., Electrical and Electronics Engineering

Supervisor : Asst. Prof. Selçuk Yerci
Co-Supervisor : Prof. Dr. Raşit Turan

January 2018, 94 pages

The state-of-the-art solar cells manufactured using crystalline silicon (c-Si) are highly cost-effective, competing with fossil fuel-based energy sources. However, relatively more complex cell structures (i.e. interdigitated back contact, IBC) need to be developed to further increase the efficiency/cost ratio.

In this thesis, the effects of structural parameters such as cell dimensions, metal contact geometry and contact resistances on the efficiency of IBC and bifacial IBC silicon solar cells were studied by numerical simulations.

Light absorption in IBC and bifacial IBC solar cells was simulated using ray optics method in Opal 2 simulation software. The extracted generation profiles were embedded into Silvaco TCAD. Efficiency (η), open circuit voltage (V_{OC}), short circuit current density (J_{SC}) and fill factor (FF) of solar cells were calculated for various device configurations.

The results showed that the usage of high quality bulk Si providing longer carrier lifetime values up to 10 ms is more effective on cell efficiency than changing

the base doping between the limits $1x10^{14}$ to $1x10^{17}$ atoms/cm^3. Furthermore, the effect of the ratio of emitter width to cell width was investigated and the optimum ratio is found to be 79%. An optimum structure for a minority carrier lifetime of 1 ms and base doping concentration of $1x10^{16}$ cm^{-3} is obtained when an emitter width of 1500 μm and a back surface field width of 300 μm is realized. Finally, the effects of contact widths of bifacial IBC solar cells on efficiency were studied. A contact coverage fraction around 20% yields the highest efficiency for a floor reflection of 30%.

Key Words: *IBC Solar Cell, Bifacial IBC Solar Cell, Silvaco TCAD, Design Optimization*

ÖZ

BİRBİRİNE KENETLENMİŞ ARKA TEMASLI SİLİKON GÜNEŞ HÜCRELERİNİN SAYISAL ANALİZİ

ACAR, Beran
Master, Elektrik ve Elektronik Mühendisliği
Tez Yöneticisi : Yrd. Doç. Selçuk Yerci
Ortak Tez Yöneticisi : Prof. Dr. Raşit Turan

Ocak 2018, 94 sayfa

Fosil yakıt temelli enerji kaynakları ile rekabet halinde olan kristal silicon (c-Si) kullanılarak üretilen en gelişmiş standart güneş gözeleri yüksek maliyet verimliliğine haizdir. Bununla birlikte, verim/maliyet oranını artırmak için daha karmaşık göze yapılarının (Örneğin, birbirine kenetlenmiş arka temaslı güneş gözeleri, IBC) geliştirilmesi gerekmiştir.

Bu tezde, göze boyutları, katkılama profilleri, metal bağlantı geometrisi ve bağlantı direnci gibi yapısal parametrelerin, IBC ve çift taraflı IBC gözelerin verimliliğine etkileri, nümerik simülasyonlar uygulanarak çalışılmıştır.

IBC ve çift taraflı IBC gözelerin ışık emme yeteneği ışın optiği yöntemini uygulayan Opal 2 optik simülatörü kullanılarak simüle edilmiştir. Elde edilen üretim profilleri elektriksel simülasyonlarda kullanılmak üzere Silvaco TCAD yazılımına

gömülmüştür. Verimlilik (η), açık devre gerilimi (V_{OC}), kısa devre akım yoğunluğu (J_{SC}) ve dolgu faktörünün (FF) değişimleri çeşitli hücre konfigürasyonları için hesaplanmıştır.

Sonuçlar, silisyum gözesinde 10 milisaniyeye kadar varan daha uzun taşıyıcı ömre sahip kaliteli malzeme kullanılmasının, gözenin temel katkılamasının $1x10^{14}$ to $1x10^{17}$ atom/cm^3 sınırları aralığında değişmesinden daha etkili olduğunu göstermiştir. İlave olarak, göze emitter genişliğinin göze genişliğine oranının etkisi de araştırılmış ve optimum oran %79 olarak bulunmuştur. Göze taşıyıcı ömrü 1 ms ve göze katkılaması $1x10^{16}$ cm^{-3} alınması durumunda optimum yapı, 1500 μm genişliğinde bir Emitter ve 300 μm genişliğinde bir BSF ile sağlanmıştır. Son olarak, çift taraflı IBC güneş gözelerinin bağlantı genişliklerinin verim üzerindeki etkileri üzerine çalışılmıştır. Sonuç olarak, %30 mertebesindeki yer yansıması değeri için, %20 bağlantı alan kaplama oranı ile en yüksek enerji verimliliği sağlanmıştır.

Anahtar Kelimeler: *Birbirine Kenetlenmiş Arka Temaslı (IBC) Güneş Hücreleri, İkiyüzlü Işımalı Birbirine Kenetlenmiş Arka Temaslı (IBC) Güneş Hücreleri, Silvaco TCAD, Dizayn Optimizasyonu*

To my dearest friends and family…

ACKNOWLEDGMENTS

Firstly, I offer my sincerest gratitude to my research advisor and official co-advisor Prof. Dr. Raşit Turan and thesis supervisor Asst. Prof. Selçuk Yerci for their encouragement, inspiration, understanding, and knowledge whilst during my graduate academic life. I am also highly honored to be one of their MS graduate candidates and for giving me the opportunity to be a member of GÜNAM family. I attribute the level of my MS degree to their informative discussions, creativeness, positive attitude toward me, patience and the excellent guidance during my study. I have learned many things from them that have helped me in both my academic and my daily life.

It is a pleasure to offer my sincere thanks to all people who helped me to carry out this research.

My deepest thanks belong to Hande Çiftpınar for her continuous encouragement and guidance throughout this research. Without her creativeness, her humor, her positive attitude, her contagious passion for IBC solar cell and its simulations, this research would be tough. She put me on the right track by the several hours she spent with me to introduce and discuss every aspect of the fascinating world of solar cells. You and all your efforts and support are not and for sure will never be forgotten!

I am highly grateful to Prof. Dr. Shahzad Hussain for his general interest in this work. Illuminating discussions we had together and his many critics have had a great impact on the high quality of the work presented in this thesis. I have acquired many scientific capacities from him. I thank Prof. Dr. Shahzad Hussain for his professionalism and his good mood every time I asked for help (very often, indeed!).

I would like to express my warm thanks to my loyal colleagues in the 'High Efficiency Group'. Dr. Fırat Es have been well experienced helpful brother and advisor for me. I thank him for his creative ideas both in academic and daily life. Gamze Kökbudak have been a very close friend and a very nice colleague from the very beginning of my research until we separated with exchange programs. Gülsen Baytemir was so nice all the time increasing the energy of the team throughout our studies and meetings. Serra Altınoluk was very helpful and understanding especially when we were using the simulation tool together with several problems during the 2 years period. Deniz Türkay have supported me with his deep knowledge especially last year when I was writing this thesis which is the period I needed help the most. Olgu Demircioğlu and Zeynep Demircioğlu were always very patient and kind. It was nice to witness the birth of their cute little princess Arya in my last year of MS studies.

I would like to thank to Umut Çaçan not only for enduring me since I have started in GÜNAM at 2015, but also his creative ideas, friendship and helping me with my professional and private life.

Merve Pınar Kabukcuoğlu have been a kind and energetic friend. I appreciate for the beautiful time we spent together with her and Gamze Kökbudak. We spent joyful time in GÜNAM and off campus.

Efe Orhan being a new member of GÜNAM seated near my desk and become my closest friend since then. Conducting research and discussions with Efe was amazing indeed.

GÜNAM would be a monotonous research center without my dear friends and colleagues. Engin Özkol, Ezgi Abacı, Ergi Dönerçark, Salar Habibpur Sedani, Çiğdem Doğru, Emel Semiz, Mustafa Ünal, Wisnu Hadibrata, Wiria Soltanpoor, Gence Bektaş, Kurtuluş Abak, Mete Günöven were all helpful, kind and holds a valuable place in my GÜNAM adventure. I am grateful to have them by my side during my study.

I am grateful to GÜNAM technicians; Yücel Eke, Nevzat Görmez, Tayfun Yıldız, Dursun Erdoğan for technical support and also to Harun Tanık, Tuncay Güngör and Buket Gökbakan for their support in administrative things in GÜNAM.

The financial support from the Scientific and Technological Research Council of Turkey (TUBITAK BIDEB-2215) is highly acknowledged.

Last but not the least I am endlessly grateful to my lovely family, my mother, my father and my sister in particular, for their unconditional love, understanding, endless support and encouragement during my 'long student' life. They have always been supportive, have always given me superior pieces of advices, and helped me to find my way.

TABLE OF CONTENTS

LIST OF FIGURES

CHAPTER 1

INTRODUCTION

Global energy demand has been rapidly increasing and the fossil fuels such as oil, gas, and coal, from which most of the energy supplied, are gradually running out. It is commonly accepted that the renewable energy sources should replace traditional non-renewable energy sources as much as possible in order to meet the increasing energy demand in the future. The renewable energy is necessary not only because of inevitable shortage of fossil fuel sources, but also to prevent the air pollution and the global warming due to high emission of carbon dioxide caused by the use of fossil fuels. Major renewable energy sources such as wind and solar power are clean, abundant and affordable, which makes them a promising alternative to the existing fossil fuels.

Among the renewable energy sources, solar energy has the greatest potential in terms of the amount available to human population, the technological flexibility and readiness for the conversion to the other energy types, and cost of the conversion technologies. With the drastic price reductions in photovoltaic systems in recent years and the demonstration of energy supply in different applications have made solar energy popular and important type of energy source. The increase in the use of solar energy systems has been more than any expectations. This trend seems to be accelerated in the coming years, and solar energy will ultimately be one of the major source of energy supply to human being.

Conversion of solar energy to electrical energy can be done in two ways: i) Solar Thermal Electricity (STE) uses the steam generated by concentrated solar radiation in classical turbine generator; and ii) Photovoltaic (PV) solar cells generates electricity by absorbing the photons falling on the cell directly. For technical and

economical reasons, PV based technologies have dominated the solar energy industry over STE technologies in recent years.

A PV solar cell is an electronic device having a simple diode structure, i.e. a p-n junction which separates the electron-hole pair created by the absorption of a photon. The separated carriers are transported to the external metal contacts on both sides of the cells and forms the electrical currents. Technical details of a PV cell will be given in the following sections in this thesis. Today, most of the photovoltaic cells (more than %90) are made of silicon crystal (c-Si) which is also major material of microelectronic industry. Some thin film alternatives based on compound semiconductors (CdTe and CuInGaSe) are also available commercially. However, their market share has been small compared to c-Si based products due to several disadvantages.

In this thesis, two new types of solar cell structures based on crystalline silicon, namely Interdigitated Back Contacted (IBC) and Bifacial IBC solar cells, are studied. The IBC solar cell structure has been developed to prevent shadowing losses. P-N junction and metal contacts are placed to the rear side of the cell structure so that the light blockage of front metal contacts in the standard cell structure is prevented. Additionally, the rear side metallization is minimized and rear illumination is allowed in Bifacial IBC solar cell structure for further photon capturing.

The IBC solar cell structure has been studied widely in literature and a highest efficiency of 25.6% [1] has been achieved by Sunpower. The optimizations in this study are performed on IBC solar cell with Si bulk with a doping value of $1x10^{16}$ atoms/cm^3 and bulk lifetime value of 1 ms. As a result of optimizations conducted by the utilization of Silvaco TCAD simulation tool, an optimum IBC structure is built satisfying those pre-selected criteria. In order to satisfy the minimum required widths of 300 μm and 100 μm for Back Surface Field (BSF) and gap regions, respectively, the emitter width of 1500 μm is found to be the optimum.

Bifacial IBC solar cell structures are also studied with similar parameters as of IBC solar cell structures. The results of rear side optimization showed that contact

coverages around 20% is required for floor reflection rates up to 30% in order to achieve maximum efficiency with the afore mentioned preselected parameters. It is also seen that as the floor reflection value decreases, the contact coverage fraction needs to be larger.

In the following section, a literature review on history of photovoltaic industry, the developments of solar cells and the general information about the parameters of solar cells are given. In Chapter 2, the device physics and solar cell modelling are discussed. The Silvaco TCAD simulation tool is introduced in Chapter 3. The simulation results of IBC and Bifacial IBC solar cell studies are provided in Chapter 4 and Chapter 5, respectively. In Chapter 6 the conclusions and future directions are given.

1.1.History of Photovoltaic Industry

French physicist Antoine-César Becquerel was the first researcher who obtained an electric current from a silver-coated platinum electrode as a result of photovoltaic effect in 1839. Following this finding, the first solar cell was built in 1883 by Charles Fritts. With the integration of silicon as a raw material in solar cells, the first cell structure giving a conversion efficiency of 6% is produced in the Bell Laboratories [3]. In 1970's, because of the oil crisis, the interest shifted towards alternative energies with a great attention on photovoltaic energy. The main problem at that time was the cost and researchers mainly focused to develop and use alternative low cost materials such as polycrystalline silicon, amorphous silicon or thin film materials. In 1990's photovoltaic industry became more popular with the understanding of the need for safe and renewable energy.

Reduction in the production costs and availability of new materials opened an area for wide variety of solar cell research. The detailed development chart of the solar cell sector created and published by National Renewable Energy Laboratory (NREL) is shown in Figure 1.1[4].

In Figure 1.1 the efficiency progresses of most common solar cell types namely, Multi-junction cells, Crystalline Silicon cells, Thin Film technologies and Emerging Fourth generation PV cells are shown.

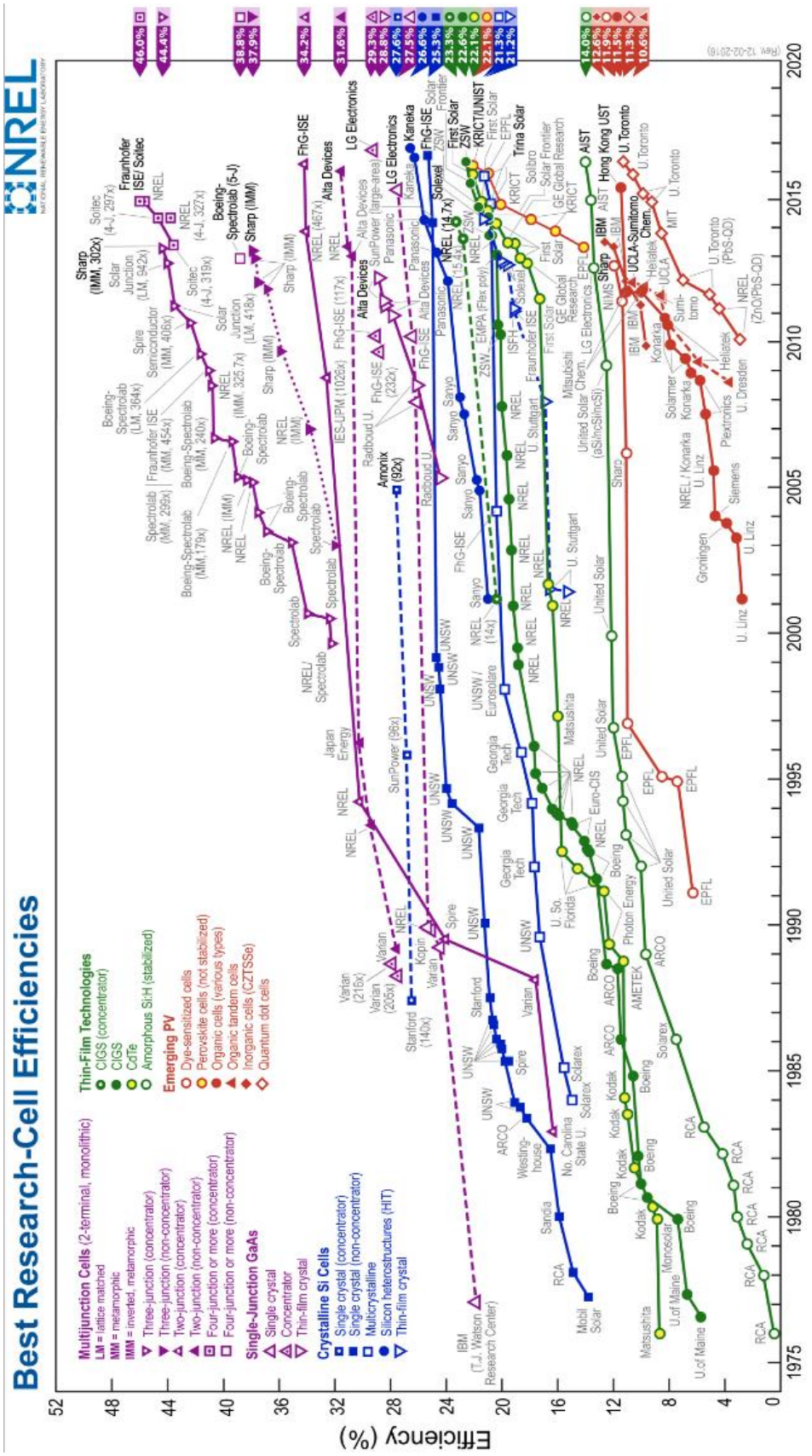

Figure 1.1: Best Research-Cell Efficiencies of NREL [4]

1.2.Solar Cell Technologies

1.2.1. Silicon Solar Cells

Silicon has been the dominating material in the solar sector since it was first noticed to be effective in solar cell production. Main reason for this domination are the low cost of the silicon, reliability and the level of maturity of the technology . Researchers studied Silicon widely as a raw material in solar cell technology because of its cost advantage. As a result, a wide variety of different silicon solar cell structures has been developed. Aluminum Back Surface Field (Al-BSF), Heterojunction with Intrinsic Thin Layer (HIT), Passivated Emitter and Rear Cell (PERC), Interdigitated Back Contacted (IBC) are the major silicon solar cell structures available commercially.

1.2.1.1. Aluminum Back Surface Field (Al-BSF) Solar Cells

The Al-BSF silicon solar cells that has the simplest structure is shown in Figure 1.2. P-type bulk is used and the front side is doped with phosphorus to form a p-n junction. Then thin SiN_x layer is deposited to decrease the reflection and to passivate the surface of the front layer. Silver paste for front contact and Aluminum paste for back contact is used. A high temperature process called firing leads to diffusion of aluminum at the backside into the silicon forming a p+ layer and thus forming a smooth and low resistive back contact. Moreover, p+ layer at the back side creates an electric field (called Back Surface Field) pushing minority carriers away from the back side of the wafer, which reduces the recombination at the back junction.

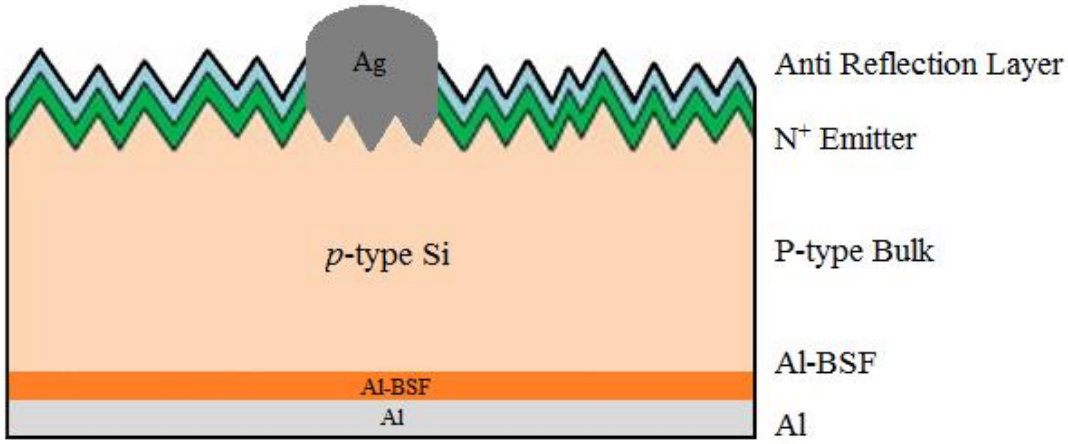

Figure 1.2: Al-BSF solar cell structure [36]

Al-BSF solar cells are easy to produce and cost efficient, so that this cell structure is very suitable for industrial mass production. Fraunhofer ISE has reached an efficiency value over 20% with Al-BSF structures which is a pretty high value for such a cheap and simple structure [5]. A similar prototype structure developed in GUNAM achieved an efficiency about 19.3%.

1.2.1.2. Passivated Emitter and Rear Cell (PERC)

PERC structure is very similar to standard Al-BSF solar cell structure. The only difference is that the back structure is not fully diffused, instead contacted locally through windows opened in a dielectric film like Al_2O_3 and Si_3N_4 by laser scribing. Electrical contacts and local BSF doping under these contacts are built in these windows while the remaining regions are passivated with a dielectric like Si_3N_4 or SiO_2 [4]. This replacement of doped and contacted regions with the passivation layer decreases the carrier recombination at the rear side of the structure. In this way the current and the fill factor of the structure is increased. These improvements have increased the efficiency up to 25% [6] making this structure one of the leading silicon solar cell design. The schematics of PERC cell is shown in Figure 1.3.

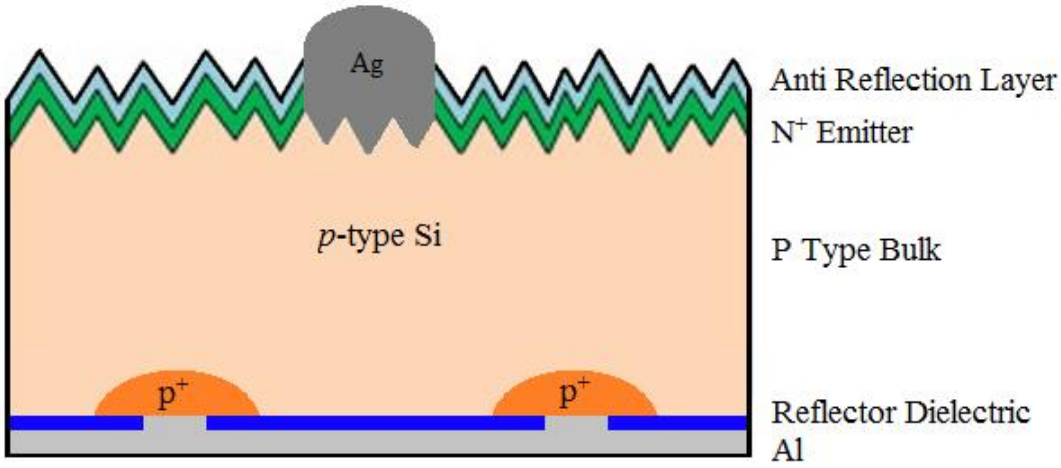

Figure 1.3: PERC solar cell structure [30]

Heterojunction with Intrinsic Thin Layer (HIT) structure employs very thin-doped amorphous silicon (a-Si) layers as carrier separator at both sides of the cell. Lightly doped crystalline silicon (c-Si) is used as the bulk and a-Si deposited to the front side is oppositely doped with the bulk so that it works as a p-n junction. Intrinsic a-Si is used at both sides of the cell to provide a smooth transfer of carriers from c-Si to metal contacts.

The advantage of HIT structure is that a-Si at both sides passivates the bulk almost perfectly decreasing the surface recombination significantly. Although the recombination in a-Si layer is very high, since very thin layers are used in the range of several nanometers these layers work as a tunneling layer. The structure is well promising and very high efficiency up to 25% [7] have been achieved. Side view of an HIT structure is shown in Figure 1.4.

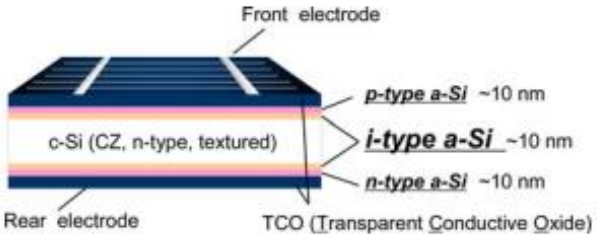

Figure 1.4: HIT Si solar cell structure [7]

1.2.1.3.Interdigitated Back Contacted (IBC) Solar Cell

Main separation of IBC structure from the others is the location of contacts. IBC is developed to prevent the optical loses due to the metal front contacts. Both the junction and the contacts are placed at the rear side of the structure but this

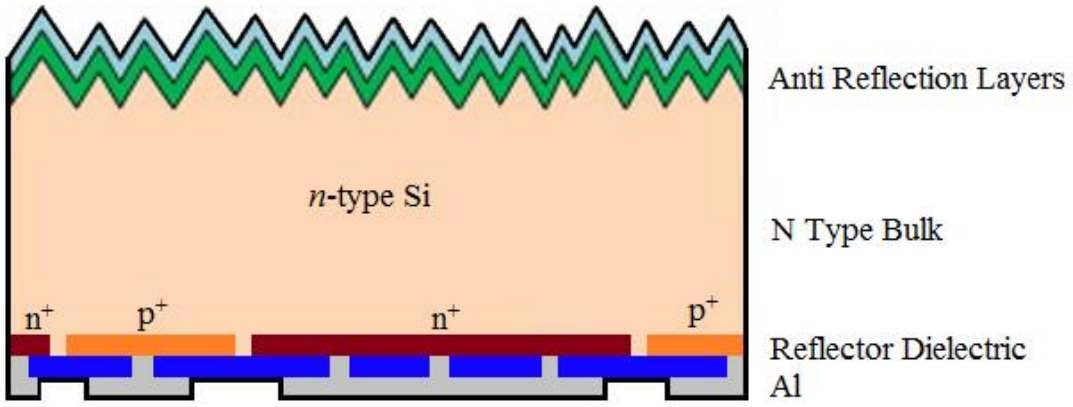

Figure 1.5: IBC solar cell structure

complicates the design of the rear structure when compared to classical design. Schematic view can be seen in Figure 1.5. Despite the complexity of the structure, IBC cell produced in this manner is properly working with high efficiency. Even more complex designs integrating different type of cells, namely Al-BSF IBC, Bifacial IBC or HIT IBC cells are also available. The Bifacial IBC structure which can be seen in Figure 1.6 is the second main structure optimized in this thesis. The highest efficiency

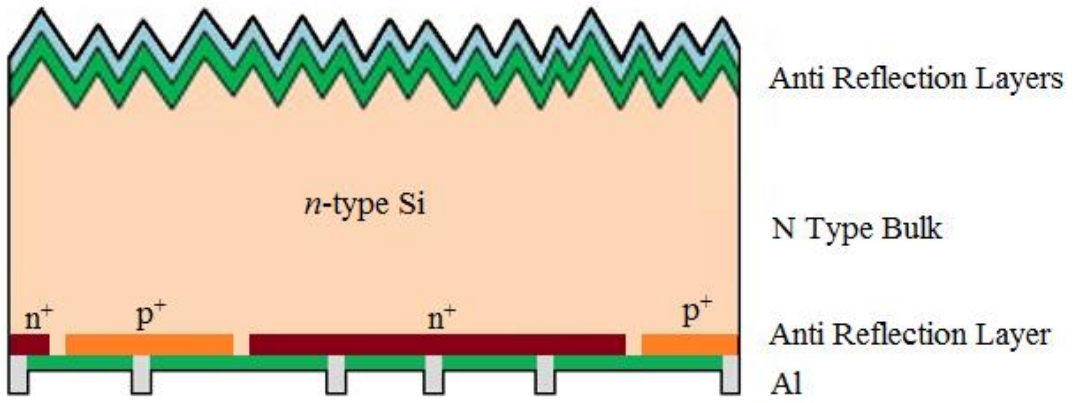

Figure 1.6: Bifacial IBC solar cell structure

value achieved so far with Silicon based solar cells is 25.6% which is produced by Panasonic [8]. The cross section of this structure is shown in Figure 1.7.

The main disadvantage of the IBC structure is that the emitter is located at the rear side. The greater part of the generation occurs at the very thin layer just below the front surface. In the standard cells, the junction at that location directly separates the majority of generated carriers. However, in the IBC structure these carriers should travel and survive long distance until they reach rear side of the structure to be

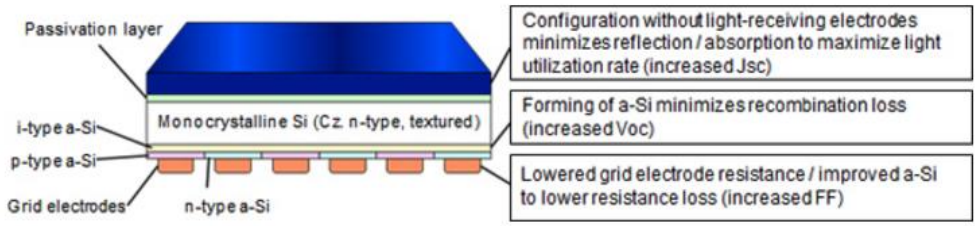

Figure 1.7: HIT-IBC solar cell structure produced by Panasonic [8]

separated by the junction. The front surface recombination and the bulk recombination are the main obstacles in this cell structure. Therefore, for a successful IBC structure the quality of the front surface passivation and the bulk lifetime should be very high. Another way of decreasing high front surface recombination is placing floating front surface field (FSF), which separates the carriers at the front and transfers minority carriers horizontally until they reach the top of the BSF.

There are some serious obstacles for the production of the IBC structures that also increase the production cost. On the other hand, highest efficiency values among the silicon cells have been achieved by IBC cell structures. IBC structure is also advantageous for panel production, since both contacts are at the rear side and they can be lined and connected easily without leaving any space between cells.

In this thesis, the optimization of an IBC structure developed at GUNAM is studied, analyzed and re-modelled for possible improvements. The detailed analysis and results are given in the “Results" section of this thesis.

1.2.2. Thin Film Solar Cells

Thin film structures are studied to decrease the material costs of silicon solar cells. It is shown that very thin solar cells are also functional, if materials with high absorption coefficients are used. The most successful thin film solar cell materials are $CuInGaSe_2$ (CIGS) and Cadmium Telluride (CdTe). The efficiencies of 19.9% [9] for CIGS and 16.5% [10] for CdTe have been achieved.

Thin film structures are produced by deposition of these active materials onto a glass or a substrate material. Only few microns of these compositions is enough to absorb all incoming light. Structures of this type are advantageous in terms of material usage but the efficiencies remain below 20%. For this reason, silicon is generally preferred for solar cell production.

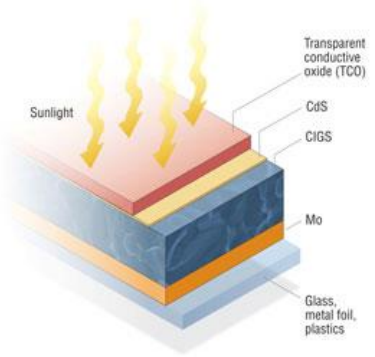

Figure 1.8: Schematics of a typical CIGS solar cell structure [38]

In Figure 1.8, an example of CIGS solar cell is shown. The absorber CIGS is deposited on Molybdenum Oxide (Mo). Transparent conductive oxide is deposited on top of the structure to provide electrical contact, to decrease light reflection and to provide passivation at the front surface.

1.2.3. Multi-Junction Solar Cell Structures

In order to exceed the theoretical limitations and reach very high efficiencies, alternative materials, device architectures have been studied. Having more than one

junctions (called tandem cells) stacked vertically is one of the most successful approaches in this direction. Tandem solar cells having efficiency conversion values over 30% are produced and some of these structures have been used for space applications. GaAs, InP, InAs materials are placed one on another to absorb light segments with different wavelengths and under concentrated light the efficiency values up to 50% [11] has been achieved. A tandem structure where GaInP layers employed for blue light absorption and GaAs layers employed for red light absorptions is shown in Figure 1.9.

.

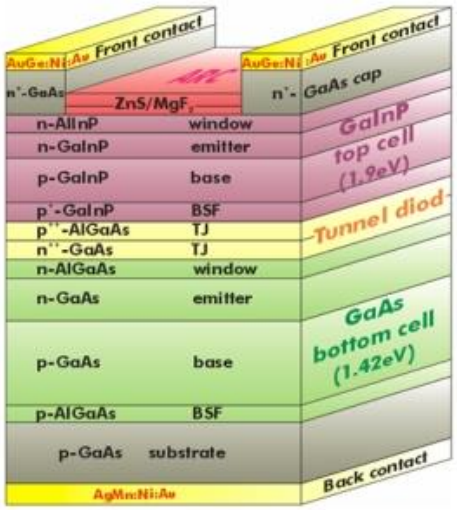

Figure 1.9: GaInP, GaAs tandem solar cell structure[39]

On the other hand, in parallel, studies to decrease the cost of cell production are conducted and many different structures are developed. For example, Dye Sensitized Solar Cells (DSSC) or organic solar cells are produced but the efficiency values remain limited and not comparable with classical approaches. Perovskite is new type of solar cell and has shown a fast development so far. Efficiencies over 17% [12] has been reached with small production costs [12] but the efficiency degradation occurs rapidly in these structures and couldn't be optimized yet.

1.3. Solar Cell I-V Characteristics

Solar cell is a p-n junction where the I-V curve of the device for illuminated and dark conditions is shown in Figure 1.10. Illumination shifts the graph downwards. The curve equation for both conditions are as follows[13],

$$I = I_0\left(e^{\frac{qV}{nkT}} - 1\right) \qquad (Eq.1)$$

$$I = I_0\left(e^{\frac{qV}{nkT}} - 1\right) - I_L \qquad (Eq.2)$$

where I, I_0, I_L are the output current, reverse saturation current and illumination current respectively. q Stands for unit charge, V represents the device voltage, k is the Boltzmann constant and the T is temperature in Kelvin. 4th quadrant carries significant data for solar cells and for better visualization the graph is converted and the calculations are done on the 1st quadrant of the converted I-V graph.

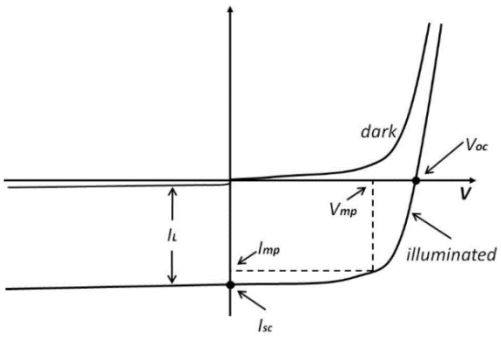

Figure 1.10: I-V curve of illuminated and dark solar cell [40]

1.3.1. Open Circuit Voltage

Open circuit voltage is the maximum amount of voltage that can be taken from the device in its solar cell operation mood that also corresponds to zero current case. The open circuit voltage point is shown on Figure 1.10. Equalizing the output current in the Eq.2 to zero we end up with the following open circuit voltage equation[13],

$$V_{oc} = \frac{nkT}{q} \ln\left(\frac{I_L}{I_0} + 1\right) \qquad \textbf{(Eq.3)}$$

1.3.2. Short Circuit Current

Short circuit current can be drawn from a solar cell by shorting the opposite contacts of the device. This current value is the maximum but valid only for zero voltage conditions. This point is shown in Figure 1.10. Setting the voltage in Eq.2 to zero we will end up with illumination current (I_L) equal to output current (I).

1.3.3. Fill Factor

The maximum power can be extracted from the device at a specific point where the multiplication of the voltage and the current gives the highest value. For a perfect device I-V curve would be rectangular and power extracted from the device would be short circuit current multiplied with open circuit voltage. However, the circular behavior at the corner of the I-V curve results in a smaller power extraction calculated by[13],

$$P_{out} = P_{mpp} = I_{mpp} V_{mpp} \qquad \textbf{(Eq.4)}$$

Where P_{mpp}, I_{mpp} and V_{mpp} are the power, current and the voltage values at the maximum power point. The I_{mpp} and V_{mpp} points can be observed on Figure 1.10. Finally the fill factor is defined as follows[13],

$$FF = \frac{V_{mpp} * I_{mpp}}{V_{oc} * I_{sc}} \qquad \textbf{(Eq.5)}$$

1.3.4. Cell Efficiency

Cell efficiency is defined as the power extracted from the solar cell divided by the input power. Which can be shown as follows[13],

$$\boldsymbol{Cell\ Efficiency\ (\eta) = \frac{P_{out}}{P_{in}} = \frac{V_{oc} I_{sc} FF}{P_{light}}} \qquad \textbf{(Eq.6)}$$

where P_{light} is the power of the incident light. Cell efficiency is the most important parameter of the cell. Main aim is to increase the efficiency as much as possible with acceptable expense. The approximate theoretical efficiency for a silicon solar cell is 30%[14]. The 70% of the incoming power is lost due to many optical and electrical losses. Efficiency of 25.6% has been reached by Panasonic[8] and the solar cell research is approaching to the practical efficiency limits of silicon solar cells. But further developments will continue for sure either to increase efficiencies further or to decrease production costs.

1.3.5. Series Resistance

Carriers which are generated and separated in the structure, passes through the semiconductor, semiconductor-metal interface and metal regions one by one facing up with resistance in each region. The total resistance in this path is called as series resistance. In detail emitter and base regions, front and rear contacts, busbars, fingers and wafer edges[15] contribute to series resistance parameter and the equation can be written as follows[15],

$$\boldsymbol{R_S = R_e + R_b + R_{c,e} + R_{c,rear} + R_{bus} + R_{fi} + R_{edge}} \qquad \textbf{(Eq.7)}$$

For a successful solar cell the series resistance should be as small as possible. The value of series resistance can be calculated numerically by taking derivative of the I-V curve at $V = V_{oc}$ point. The effect of series resistance on the diode equation of the solar cell can be observed in the following equation[13],

$$I = I_L - I_0\left(e^{\frac{qV+IR_S}{kT}} - 1\right) \qquad \textbf{(Eq.8)}$$

1.3.6. Shunt Resistance

Shunt resistance is the resistance value between the positive and negative contacts. It is expected to be very large for a proper cell, otherwise there is an undesired alternative path for carriers to complete the circuit. The possible reason for small shunt resistances is manufacturing failures. Edge isolation is one of the main technics for increasing the shunt resistance by preventing the edge leakages. The shunt resistance can be determined from the derivative of I-V curve at V = 0 point and the effect of the shunt resistance on the diode equation of the solar cell can be observed in the following equation[13],

$$I = I_L - I_0\left(e^{\frac{qV}{kT}} - 1\right) - \frac{V}{R_{SH}} \qquad \textbf{(Eq.9)}$$

CHAPTER 2

FUNDAMENTALS OF DEVICE PHYSICS AND ELECTRICAL MODELING OF SOLAR CELLS

Production of a solar cell primarily focuses on absorbing the maximum number of photons available since more photons means more carriers produced in the bulk to be collected at the contacts. For an efficient solar cell, the reflection should be very small, the conversion efficiency should be high and the collection of carriers and transportation of the energy should be efficient. Considering these factors, the losses can be categorized in three main titles for crystalline silicon solar cells which are electrical losses, carrier losses and photon losses. The visualizations of the loss mechanisms can be observed on Figure 2.1.

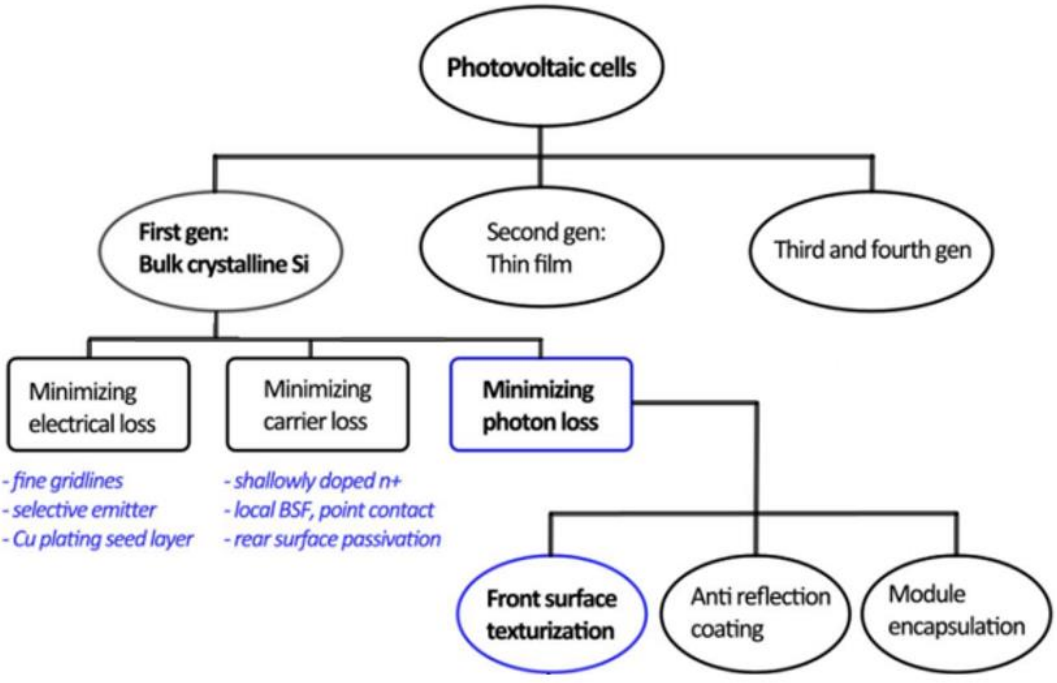

Figure 2.1: Classification of Loss mechanisms in Si-based Solar Cells

Silicon with its bandgap at 1.12 eV[13] is not the optimum material for PV industry since it does not absorb the sunlight as efficient as other materials do and Si based solar cells are 10 or 100 times ticker when compared to cells with other materials such as GaAs. Moreover photons having less energy than the band gap of a semiconductor could not be absorbed to create electron hole pairs in the semiconductor device and the incident light portion having a wavelength greater than 1100 nm could not be absorbed by silicon since the photons have energy smaller than 1.12 eV over that wavelength.

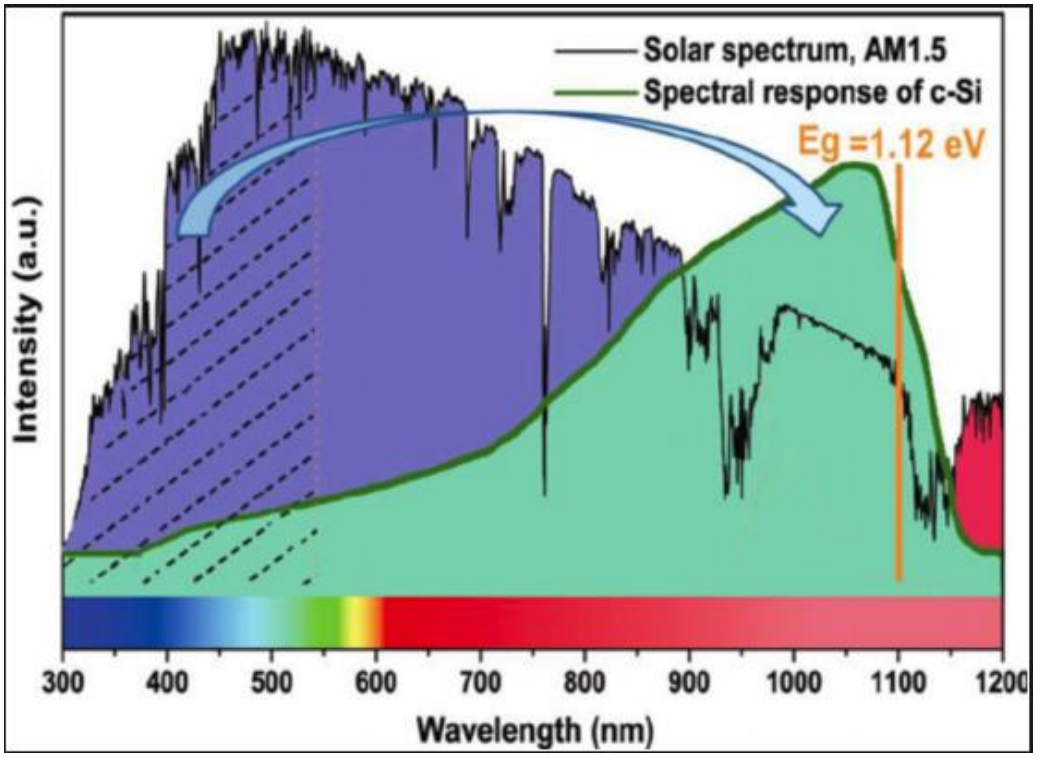

Figure 2.2: Solar spectrum and Si spectrum for comparison[13]

On the other side, photons with shorter wavelengths supplies much higher energy to e^--h^+ pairs than needed such that the excess energy is lost in the lattice with the process called "Thermalization"[16]. Thermalization losses in the small wavelength region and non-absorbed photons in the long wavelength region are the results of the difference between the absorption spectrum of Si to the incident spectrum at AM1.5 conditions, which is called the "spectral mismatch". The AM1.5 spectrum and spectral response of c-Si is shown in Figure 2.2.

2.1.Optical Properties

Optical properties occupies a significant role when the quality and efficiency of a solar cell is discussed. Optical losses forms more than 30% of all losses in a solar cell [17] structure. There are number of techniques developed and being used to decrease optical losses of a solar cell.

Very thin Si nitride or SiO_2 layer on top of the structure is used to prevent the reflection from the front surface and the layer has given the name anti reflection coating (ARC). Texturing is another technique to trap the light in to the structure and increase the number of light-surface interactions. Both techniques are given in detail in the following sections. An option to increase the long wavelength (red portion of the spectrum) absorption is to increase the depth of the structure since the red light propagates long distances in the Si. Some designs such as IBC structure have their both contacts placed at the rear side of the cell in order to avoid the shadowing losses as a result of the reflection from the front metal contacts. In Figure 2.3 the different paths followed by the incoming rays and the sources of the optical losses can be observed.

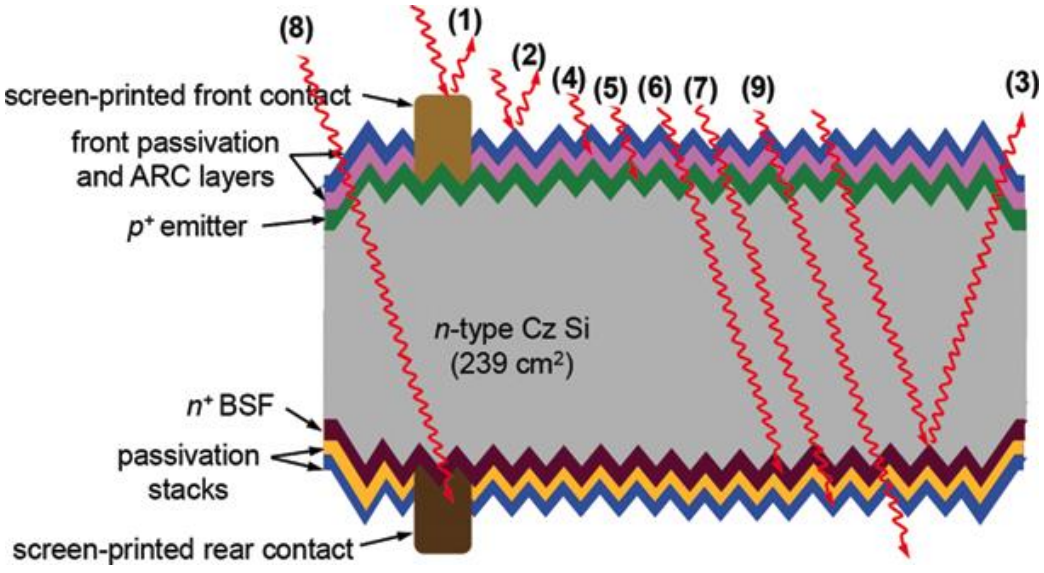

Figure 2.3: Optical losses of solar cells [14]

2.1.1. Texturing

Increasing the absorption of the long wavelength region of the spectrum is possible by increasing the distance travelled by light in Si. Red light (long wavelength photons) travels a long distance before being absorbed in Si. Thicker cells seems as the solution but the cost increases as the thickness increases , also the carriers will recombine in higher rates as they travel long distances before reaching contacts. The solution is to increase the optical distance without changing the cell thickness that is possible by light trapping. If we successfully keep the incoming light entering the structure inside the wafer by forcing it travel longer distances than the depth of the solar cell than this operation is called as light trapping[18]. Texturing is one of those main strategies to increase the optical distance by diffracting the incoming light and blocking the outgoing light.

Texturing is very common and simple process generally obtained by potassium hydroxide (KOH) or sodium hydroxide (NaOH) solutions that etches the surface of the Si to form small pyramids. Light interacts with pyramid covered surface more than once, which decreases the reflection rate from the surface. Reflection parameter R is a value between 0 and 1 numerically and the total reflection from a pyramid covered surface will be R^2 in case of 2 interactions which decreases the total reflected portion significantly.

2.1.2. Anti Reflection Coating

Anti Reflection Coating (ARC) is a thin dielectric layer deposited on to the front surface of solar cells. Generally SiNx or SiO_2 depositions are used for Si solar cells[19]. Without ARC layers the reflection, transmission coefficients and reflectance, transmittance equations of Si surface at normal incidence are given below[13],

$$\boldsymbol{r = \frac{n_0 - n_i}{n_0 + n_i}} \qquad \textbf{(}\boldsymbol{Eq}\textbf{.10)}$$

$$t = \frac{2n_0}{n_0 + n_1} \qquad \textbf{(Eq.11)}$$

$$R = |r|^2 = \left|\frac{n_0 - n_i}{n_0 + n_i}\right|^2 \qquad \textbf{(Eq.12)}\ [13]$$

$$T = \left|\frac{n_1}{n_0}\right| |t|^2 = \frac{4|n_0 n_1|}{|n_0 + n_1|^2} \qquad \textbf{(Eq.13)}$$

where n_0 and n_1 represents the complex refractive indices of first and second medium.

Bare Si reflects approximately 40% of the incoming light [20]. Anti-reflection coating is used to provide a smooth transfer for the incoming rays through the interface.

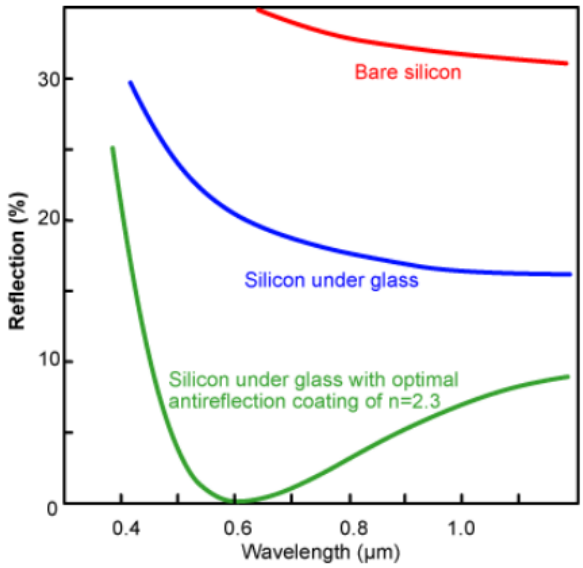

Figure 2.4: Reflection graphs of bare Si in comparison with ARC coated Si and Si under glass

The reflectance at normal incidence is modified as in the following equation after the ARC deposition[13],

$$R = \frac{(n_0 - n_i)^2 + \left(\left(\frac{n_0 n_s}{n_1}\right) - n_1\right)^2 \tan^2 \delta_1}{(n_0 + n_i)^2 + \left(\left(\frac{n_0 n_s}{n_1}\right) + n_1\right)^2 \tan^2 \delta_1} \qquad (Eq.14)$$

where δ_1 represents the phase shift of the ARC layer and expressed as in[13],

$$\delta_1 = \frac{2\pi n_1 d_1 \cos\theta_1}{\lambda} \qquad (Eq.15)$$

where θ_1 is the angle between the incoming light with the normal of the surface.

When anti reflection coating is added to the structure the reflectance can be minimized by equalizing $\delta 1 = pi/2$. d_1 has to be one quarter of the wavelength in the film so that light reflected from 2 surfaces will be out of phase. Another way of minimizing the R is taking the refractive index of ARC as the geometrical average[13],

$$n_1 = \sqrt{n_0 n_s} \qquad (Eq.16)$$

Refractive index of Si is approximately 3.3 around 600nm[21] and taking the index for air 1 the optimum refractive index for ARC layer becomes $n = \sqrt{3.3} = 1.81$. The refractive index of SiNx can be arranged around 1.81 so it is the optimum ARC layer for Si solar cells.

2.1.3. Shading Effect of Front Metallization

Metal contacts are required to collect the generated electron hole pairs. Traditional designs have contacts at the both sides collecting carriers with opposite signs. However, the contacts at the front side blocks approximately 5% of the incoming light [22]. Despite being a small loss, after a point, researchers moved their focus towards improving these small effects to get close to theoretical limits as much

as possible. Different ideas come up and some of them changed the structure totally to get rid of these shadowing losses. Interdigitated Back Contacted (IBC) solar cells are a result of one of these ideas. Both anode and cathode contacts are taken to the rear side of the cell so that there is no metal coverage left in the front side. Shadowing effect is eliminated with this approach.

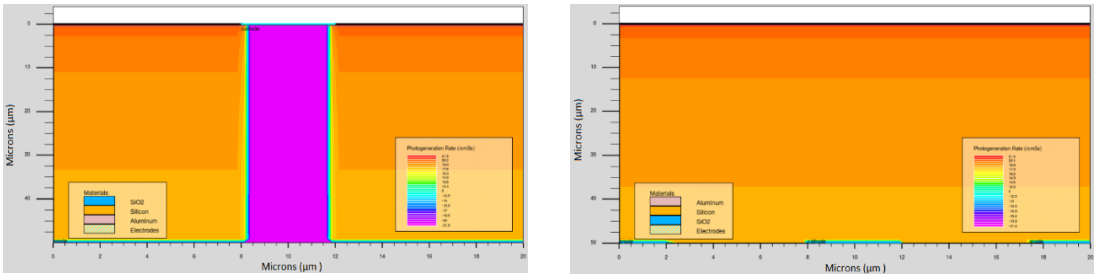

Figure 2.5: Generation profiles of: (a) 2-sided classic solar cell, (b) IBC solar cell

In Figure 2.5 the generation profiles of the 2-side contacted and interdigitated back contacted solar cells are given for ease of comparison. These models show clearly the extra illuminated region when the emitter is also placed to the rear side.

2.1.4. Optical Models

2.1.4.1. Ray Tracing (RT)

Ray Tracing is one of the simplest optical simulation models. Ray Tracing optical model is used in this thesis as well. It mainly ignores the wave nature of light and draws straight paths to rays passing through interfaces. The reflected and transmitted portions are calculated according to Fresnel equations[23] and the incoming rays are separated into two at each interfaces. After this interaction the system traces both of these rays. The simplified Fresnel equations incorporating with Snell's Laws are as follows[23],

$$r_p = -\frac{\tan(\theta_i - \theta_t)}{\tan(\theta_i + \theta_t)} \qquad (Eq.17)$$

$$t_p = \frac{2\sin\theta_t \cos\theta_i}{\sin(\theta_i + \theta_t)\cos(\theta_i - \theta_t)} \qquad (Eq.18)$$

$$r_s = -\frac{\sin(\theta_i - \theta_t)}{\sin(\theta_i + \theta_t)} \qquad (Eq.19)$$

$$t_s = \frac{2\sin\theta_t \cos\theta_i}{\sin(\theta_i + \theta_t)} \qquad (Eq.20)$$

where r_p and r_s stands for the reflection of p polarized and s polarized rays, and t_p and t_s stands for the transmission of p polarized and s polarized rays. The θ_i and θ_t represents the angles with respect to the normal of the surface for the incoming and the transmitted light. The interaction of the incident ray with an interface can be observed on Figure 2.6.

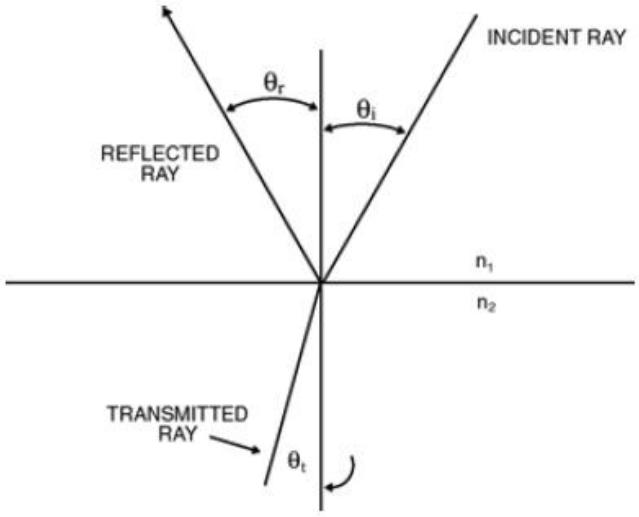

Figure 2.6: Angles of incidence, reflection and transmission[28]

In the same figure the reflected and transmitted rays can be also seen each given with their angles with respect to the normal of the surface. The angles given in the equations are visualized in Figure. The refraction index n_1 of the top medium is smaller than the refraction index n_2 of the bottom medium so that the transmitted ray approaches to the normal of the interface.

2.1.4.2. Ray Tracing Utilized in OPAL 2

In generic ray tracing programs, each ray is treated individually; reflection, absorption and transmission data's are calculated for each of them. Most of the rays follow the same paths with similar angles and number of interactions. The approach in OPAL 2[24] optical simulation tool uses this idea to reduce the calculation time[25].

Incoming ray heading towards to a textured surface interacts with the surface either 2 or 3 times. All incoming rays hit the structure with at 54.74^{o} and the 88.9% of the time the second interaction happens with an angle of 15.79^{o}. The remaining 11.1% of the rays hit the same facet 2nd time with an angle of 86.32^{o}[25].

The OPAL 2[24] is built on to this information and the Fresnel equations are utilized only for 2 times for this structure and the results are used for each ray following the same path. For other examples rays maybe separated in greater number of groups but the same equations will not be solved for each ray interaction for sure. This simplification decreases the simulation time significantly.

OPAL 2 allows the user to select a light trapping model. An equation for the parameter Z, which is the "optical path length enhancement factor", is chosen and used in the following absorption equation [24],

$$\boldsymbol{A = e^{-\alpha Z W}} \qquad \textbf{(Eq.21)}$$

where α is the absorption coefficient, W is the thickness of the substrate. There are different approximate equations for the Z parameter but in this study the detailed equation suggested by Martin Green[26] is used which is as follows[26],

$$\boldsymbol{Z = 4 + \frac{\ln[n^2 + (1 - n^2)e^{-4\alpha W}]}{\alpha W}} \qquad \textbf{(Eq.22)}$$

Using this model, an approximate generation profile is obtained from the OPAL 2 simulator and inserted into the Silvaco TCAD for further electrical simulations and optimizations of the IBC cell.

There are many detailed models for simulating the optical properties of semiconductors and solar cells, general information about main models in the literature is given in the following subsections.

2.1.4.3. Characteristic Matrix and Transfer Matrix Method (TMM)

To explain transfer matrix method we should first mention the characteristic matrix of a layer. Characteristic matrix of a layer relates the tangential components of the electric and magnetic fields at layer boundaries. Multiplying characteristic matrices of layers, one reaches the characteristic matrix of the multilayer structure. This characteristic matrix includes all optical properties of the multilayer also depending on some external factors such as angle of incidence. On the other hand transfer matrix relates the electric field amplitude of the incident light directly to the transmitted and reflected waves using Fresnel equations.

For multilayer structures with many thin layers, it is sufficient to calculate reflectance and transmittance. On the other hand, for thick films the light intensity distribution should be calculated. For this purpose Maxwell equation solving models can be used resulting in an expensive calculation times but with a higher precision or still we can use transfer matrix method with acceptable calculation time but with the following regulations:

- ✓ Layer thicknesses are much smaller than lateral distances of the device
- ✓ Incident light is parallel to or separated with very small angle from the surface normal
- ✓ No backward running wave behind the layered medium exists

These regulations are needed because TMM is one-dimensional approach and solves one dimensional Helmholtz[27] equations rather than Maxwell equations. For

thin layers it results in a much faster calculation time with proper assumptions so it becomes the right choice for solar cells with thin ARC layers at their front sides.

2.1.4.4. Monte Carlo Ray Trace (MC)

Monte Carlo ray trace is suitable for random textured solar cells. Probabilistic reflection and transmission calculations done as in Ray Trace model, but the ray to be traced will be picked randomly to be reflected or transmitted. Since it is a random process and it only continues calculations with the chosen rays for the same initial number of rays the calculation time is much smaller but the precision also decreases significantly. For reaching the same results precisely the initial number of rays should be larger than the other approaches. On the other hand, this random process decreases the simulation time significantly despite using much rays than the other approaches.

2.1.4.5. Finite Difference Time Domain (FDTD)

Finite Difference Time Domain method is the most detailed and time consuming method between these optical models. FDTD solves the fundamental Maxwell equations to calculate electric and magnetic field propagations. It includes reflection, diffraction and interference effects and performs full analysis for the light interactions. For non-planar multilayer structures FDTD can be considered but it is not used since it is much expensive from time aspects.

2.2. Device Physics

Solar cell is an electronic device that converts energy of light coming from sun in to the electrical energy. In this chapter, first the semiconductor physics is explained then the working principles of solar cells are mentioned in detail.

2.2.1. Basic Semiconductor Equations

Following the deep research related to device physics and semiconductors, today it is possible to model the operation of any semiconductor device. A couple of fundamental equations forms the basis of this model. These equations are derived

from Maxwell's laws and they consists of Poisson's equation, continuity equations and transport equations. These equations link together the electrostatic potential and carrier densities and describes the determination of electron and hole densities according to transport, generation and recombination processes. These equations will be given and the mathematical models used in Silvaco TCAD simulation tool will be introduced in this chapter.

2.2.1.1. Poisson's Equation

Poisson's Equation gives the relation between the electrostatic potential (ψ) and the space charge density (ρ) with the following equation[13],

$$\boldsymbol{div(\varepsilon \nabla \psi) = -\rho} \qquad \textbf{(Eq.23)}$$

where ε is the local permittivity of the environment. The local space charge density represents all the mobile and fixed charges including carriers (e^- and h^+) and ionized impurities.

2.2.1.2. Carrier Continuity Equations

The continuity equation for carriers in a semiconductor is given as[28],

$$\boldsymbol{\frac{\partial n}{\partial t} = \frac{1}{q} div\overrightarrow{J_n} + G_n - R_n} \qquad \textbf{(Eq.24)}$$

$$\boldsymbol{\frac{\partial p}{\partial t} = -\frac{1}{q} div\overrightarrow{J_p} + G_p - R_p} \qquad \textbf{(Eq.25)}$$

where n and p are the electron hole concentration, J represents the current densities, G represents the generation rates and R represents the recombination rates for the corresponding carriers. The electron charge is represented by q.

2.2.1.3. Transport Equations and Drift-Diffusion Model

Boltzmann Transport Equations form the basis of transport models. Usually some approximations or simplifications are applied to these equations for ease of calculation and different transport models exists. Drift-Diffusion model is the one utilized in this study.

Drift-Diffusion model is the simplest one when compared to other much complex models such as Energy Balance Transport Model or hydrodynamic model. In drift-diffusion model only independent variables introduced are the electrostatic potential ψ and carrier densities n and p. Unless the device has very small feature sizes this model has acceptable approximations and it is the model which is used in this thesis for electrically modelling the solar cell structures precisely.

In drift-diffusion model the current densities are expressed as follows[28],

$$\overrightarrow{J_n} = q\mu_n nE + qD_n \nabla n(x) \qquad \textbf{(Eq.26)}$$

$$\overrightarrow{J_p} = q\mu_p pE - qD_p \nabla p(x) \qquad \textbf{(Eq.27)}$$

where μ_n and μ_p are the electron, hole mobilities, E is the electric field, D_n and D_p are the diffusion coefficient for holes and electrons respectively. Through the Boltzmann approximations the quasi Fermi levels are linked to the carrier concentrations as follows[28],

$$n = n_{ie} \exp\left[\frac{q(\psi - \phi_n)}{kT_L}\right] \qquad \textbf{(Eq.28)}$$

$$p = n_{ie} \exp\left[\frac{-q(\psi - \phi_p)}{kT_L}\right] \qquad \textbf{(Eq.29)}$$

where n_{ie} is the effective intrinsic concentration and the T_L is the lattice temperature. Rewriting these equations defines the quasi-Fermi potentials as follows[28],

$$\phi_n = \psi - \frac{kT_L}{q} ln \frac{n}{n_{ie}} \qquad (Eq.30)$$

$$\phi_p = \psi - \frac{kT_L}{q} ln \frac{p}{n_{ie}} \qquad (Eq.31)$$

Effective electric fields are defined as follows[13],

$$\overrightarrow{E_n} = -\nabla \left(\psi + \frac{kT_L}{q} \, lnn_{ie} \right) \qquad (Eq.32)$$

$$\overrightarrow{E_p} = -\nabla \left(\psi - \frac{kT_L}{q} \, lnn_{ie} \right) \qquad (Eq.33)$$

which allows us to write the current density in a more conventional way as is shown in the following equations[28],

$$\overrightarrow{J_n} = q\mu_n n\overrightarrow{E_n} + qD_n \nabla n \qquad (Eq.34)$$

$$\overrightarrow{J_p} = q\mu_p p\overrightarrow{E_p} + qD_p \nabla p \qquad (Eq.35)$$

For this derivation of the drift-diffusion model it is assumed that the Einstein relationship holds.

2.2.2. Basic Theory of Carrier Statistics

2.2.2.1.Fermi-Dirac and Boltzmann Statistics

The Fermi-Dirac statistics are valid for the electrons in thermal equilibrium at a temperature T_L in a semiconductor lattice. Statistics based on the use of Eq.27 are referred to as Fermi-Dirac statistics. The $f(\varepsilon)$ is the probability of occupation of an available electron state with energy ε[28],

$$\boldsymbol{f(\varepsilon) = \frac{1}{1 + \exp\left(\frac{\varepsilon - E_F}{kT_L}\right)}} \qquad \textbf{(Eq.36)}$$

where E_F is spatially independent reference energy which is known as the Fermi level and k represents the Boltzmann's constant.

This equation can be approximated as in Eq.28 in case of $\varepsilon - E_F >> kT_L$[28],

$$\boldsymbol{f(\varepsilon) = \exp\left(\frac{E_F - \varepsilon}{kT_L}\right)} \qquad \textbf{(Eq.37)}$$

Calculations made by the use of Eq.28 gives us the Boltzmann statistics. Usage of Boltzmann statistics may result in some inaccuracy for very highly doped (degenerate) materials. For the rest of the calculations, using Boltzmann statistics will be much logical considering the decrease in the calculation time.

2.2.2.2. Effective Density of States

Electron and hole concentrations can be calculated by integrating the Fermi-Dirac statistics over a parabolic density of states in the conduction and valence bands. Considering the approximation in Eq.26 is good enough the electron and hole concentrations are given as follows[28],

$$\boldsymbol{n = N_C \exp\left(\frac{E_F - E_C}{kT_L}\right)} \qquad \textbf{(Eq.38)}$$

$$\boldsymbol{p = N_v \exp\left(\frac{E_V - E_F}{kT_L}\right)} \qquad \textbf{(Eq.39)}$$

where N_C and N_V are the effective density of states in the conduction band and valence band respectively. The values of N_C and N_V for Si at 300 K is as follows[28],

$$\boldsymbol{N_C = 2.82\ x\ 10^{19}} \qquad \textbf{(Eq.40)}$$

$$N_V = 1.83\ x\ 10^{19} \qquad \textbf{(Eq.41)}$$

2.2.2.3. Intrinsic Carrier Concentration

Intrinsic carrier concentration is the multiplication of electron and hole concentrations[28],

$$np = n_{ie}^2 \qquad \textbf{(Eq.42)}$$

Multiplying the Eq.29 and Eq.30 we end up with the following equation for intrinsic carrier concentration[28],

$$n_{ie} = \sqrt{N_C N_V}\,\exp\left(\frac{-E_g}{2kT_L}\right) \qquad \textbf{(Eq.43)}$$

where $E_g = E_C * E_V$ is the band gap energy. For intrinsic semiconductor the electron and hole concentrations are equal and from Eq.29 and Eq.30 the E_i Fermi level for intrinsic Si can be calculated as follows[28],

$$E_F = E_i = -q\psi_i = \frac{E_C + E_V}{2} + \frac{kT_L}{2}\ln\left(\frac{N_V}{N_C}\right) \qquad \textbf{(Eq.44)}$$

where ψ is the intrinsic potential. The electron and hole concentrations are expressed in terms of the intrinsic concentration as follows[28],

$$n = n_{ie}\exp\left[\frac{q(\psi - \phi_n)}{kT_L}\right] \qquad \textbf{(Eq.45)}$$

$$p = n_{ie}\exp\left[\frac{-q(\psi - \phi_p)}{kT_L}\right] \qquad \textbf{(Eq.46)}$$

where ϕ is the potential corresponding to the Fermi level.

2.2.2.4. The Universal Energy Bandgap Model

The Bandgap energy at temperature T_L is modeled as follows [13],

$$E_g(T_L) = E_g(0) - \frac{E_{g\alpha} T_L^2}{T_L + E_{g\beta}} \qquad \textbf{(Eq.47)}$$

where T_L is the temperature, $E_{g\alpha}$ and $E_{g\beta}$ specifies the alpha and beta coefficients for temperature dependence of bandgap and $E_g(0)$ is the band gap energy at zero calvin.

2.2.3. Basic Solar Cell Operation

Si is used as the absorbing material, and in the standard cell structure the front side is doped with the opposite dopant of the base, so a p-n junction can be obtained at the front side of the cell. The absorbed photons generate electron-hole pairs in the bulk and these carriers diffuse in the structure. The junction separates carriers with the help of electric field formed in the depletion region because of the immobile ionized dopant atoms that is explained in "P-N Junction Operation" section. This separation helps and provides the collection of carriers at the contacts before the recombination takes place. Basic structure is shown in Figure 2.7.

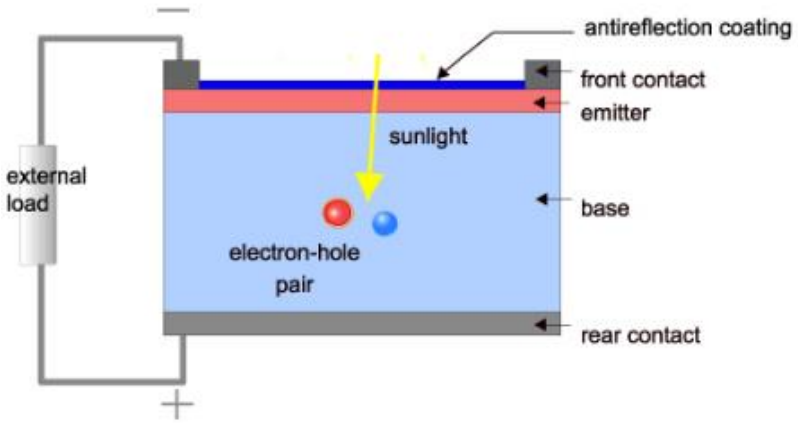

Figure 2.7: Simple structure of a solar cell[15]

To improve the cell efficiencies modern cells have anti-reflection coatings and textures on their front surfaces to increase the light trapping, these modifications are mentioned in detail at "Optical Properties" section. Majority carriers of the bulk are

collected at the back contact where minority carriers move to front side to be collected at the front contacts. As the carriers are collected at the contacts they meet each other at the load so that the circuit is completed transferring the energy to the load. There are also other cell structures having both contacts at the rear side which are named as “Interdigitated Back Contacted (IBC) Cells” which is the structure to be optimized in this study.

2.2.4. Absorption and Carrier Generation

The carrier generation is the second step following light absorption for the conversion of the light energy into the electrical energy. For carrier generation the incident photon should be absorbed in the absorber region. For this operation the photon should have an energy equal to or larger than the band gap energy of the absorber material. Photons having energy less than band gap energy passes through the semiconductor as if it were transparent and forms the transmission losses of the structure.

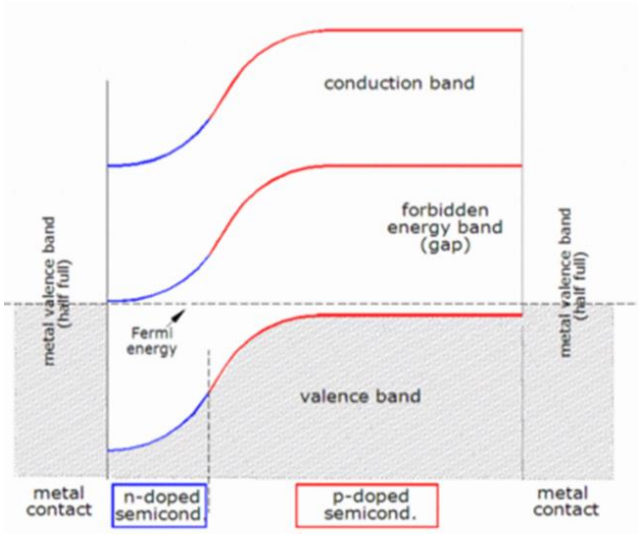

Figure 2.8: Band gap visualization of solar cell[41]

Also light trapping structures and layers are needed especially in the front side of the cell not to lose any portion of the incident light with reflection. At the optical properties chapter the optimum front structure is given for proper light trapping.

When a photon is absorbed in the solar cell, it generates electron-hole pair. In an extrinsic semiconductor, the number of electrons and holes are determined by the number of dopants in the crystal. Inmost of the cases, the photo-generated carriers are less than the majority carriers (electrons in n-type Si, holes in the p-type Si). On the other hand, minority carrier density without any photo-generated carriers is much smaller than generation rate so that during generation the minority carrier density can be approximated by photo-generated carriers.

Absorption does not occur in the same rate for different materials. Absorption constant is the parameter that determines how far the incident light can travel in the structure. This value is different for each material and also changes according to the wavelength of the incident light. For wavelengths having energy below the band gap of the semiconductor the absorption coefficient becomes 0. For higher photon energies, the coefficient is not constant and it increases as the energy of the incident light increases.

Absorption coefficient α can be expressed as follows in terms of extinction coefficient, k and wavelength, λ [13],

$$\boldsymbol{\alpha = 4\pi k/\lambda} \qquad \textbf{(}\boldsymbol{Eq}\textbf{.48)}$$

The distance covered by the incident light in the semiconductor is expressed by the absorption depth. Mathematically, absorption depth is the distance where the light intensity drops to 36% of its initial value. Also it is equal to α^{-1} and since absorption coefficient for high energy light is very high, small wavelength light is absorbed in very short distances, for example blue light is absorbed in few microns of a Si solar cell whereas the red light can pass through a hundreds micron thick Si structures.

Light intensity decrease can be calculated from the equation below for each wavelength with a different absorption coefficient value[13],

$$I = I_0 e^{-\alpha x} \qquad \textbf{(Eq.49)}$$

where I_0 is the initial light intensity, x is the traveled distance in the semiconductor and I is the light intensity at the traveled distance.

As the photons are absorbed in the semiconductor, electron hole pairs are generated in the structure with the energy of photons. Integrating the light intensity equation we can end up with the generation profile equation depending on the absorption coefficient as follows[13],

$$G = \alpha N_0 e^{-\alpha x} \qquad \textbf{(Eq.50)}$$

where N_0 refers to the photon flux at the surface and x corresponds to the depth for the corresponding generation value. This equation gives the generation profile of incident light with a single wavelength and to reach the generation rate in a solar cell we are summing up the individual carrier generations of all wavelengths in the solar spectrum. Also this equation shows that the light intensity decreases exponentially in a semiconductor so the highest generation can be obtained at the front surface of the device.

2.2.5. Carrier Recombination

Recombination is the loss of electron-hole pairs in a semiconductor through different interactions. Auger and Shockley-Read-Hall recombination's are the main recombination types in solar cells. Auger recombination occurs especially in high doped regions since the energy released by the recombination is transferred to another electron in the conduction band. In case of light doping, small number of electrons in the conduction band decreases the possibility of auger recombination[29]. Doping should be arranged carefully in order not to limit the efficiency of the cell because of the high auger recombination values.

Shockley-Read-Hall (SRH) recombination which is the integration of the electron-hole pairs through trap states, does not occur in pure semiconductors. Traps in the bulk function as a step between the hole at the valence band and the electron at the conduction band. Recombination decreases as the quality of the material increases. This recombination under low injection assumption is expressed as follows for p-type and n-type structures[30] respectively [13],

$$U_n = R_n - G_n = \frac{n_p - n_{p0}}{\tau_n} \qquad \textbf{(Eq.51)}$$

$$U_p = R_p - G_p = \frac{p_n - p_{n0}}{\tau_p} \qquad \textbf{(Eq.52)}$$

where U, R, G are the net carrier change, recombination, generation parameters and τ is the average time an excess carrier recombines.

Radiative recombination is another recombination type which is dominant in the direct band gap semiconductors, simply electrons and holes merges releasing energy in form of light. For Si radiative recombination is negligible.

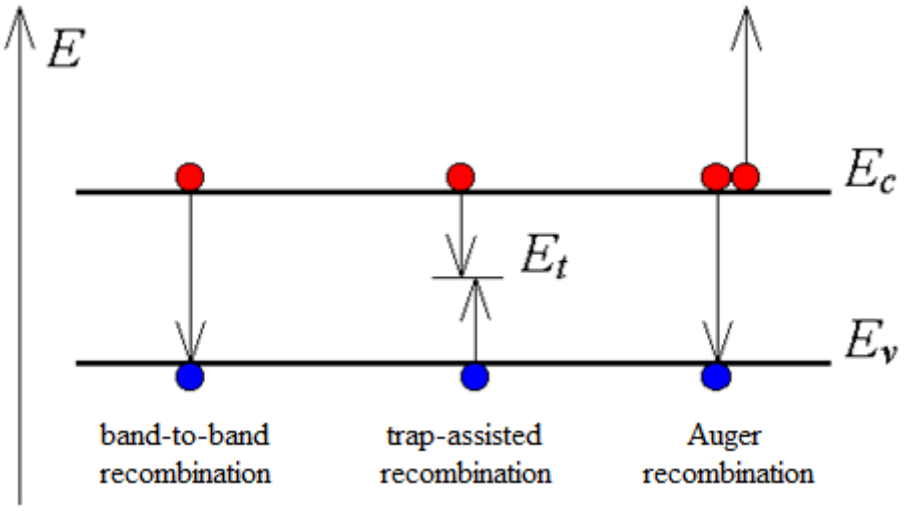

Figure 2.9: Recombination types in the semiconductors [8]

Finally, surface recombination is the other important carrier loss mechanism in the solar cells. Since the periodicity of the lattice structure is interrupted in the surface, trap states are formed because of the dangling bonds. These bonds can be filled with some passivation techniques but especially for thin cells surface recombination may stay as an efficiency limiting factor. In Figure 2.9 the recombination types are visualized.

2.2.6. Carrier Transport and P-N Junction Operation

2.2.6.1. Zero Current Conditions

The movement of carriers in a semiconductor is possible if there are free carriers in the structure which are the electrons in the conduction band and the holes in the valence band. These carriers move in random directions in the lattice structure of the semiconductor and they travel an average distance called scattering length. Then they collide with a lattice atom and go on their movement through another random direction. The average velocity of the carriers is called the thermal velocity and determined with the temperature. Each carrier makes a random motion with a velocity close to thermal velocity but in the big picture it is shown that there is no net motion of carriers in the structure. Basically a motion of a carrier is compensated with other carriers moving in the opposite direction resulting with a zero net replacement of carriers in the structure. This condition is called as zero current condition and it is valid if there is no electric field or a concentration difference in the structure.

2.2.6.2. Diffusion Current

If carrier concentration of a region is much higher or lower than its surrounding then the random motion of carriers results in a net movement of carriers to equalize the concentrations in these regions. This net movement of carriers is called diffusion. The rate of diffusion is determined by the velocity of the carriers so that with higher temperatures the diffusivity is also large. Diffusion current of electrons and holes in a semiconductor is given in the following expression [13],

$$I_{Diffusion} = qAD_n \frac{dn}{dx} - qAD_p \frac{dp}{dx} \qquad \textbf{(Eq.53)}$$

where q is the unit charge, A is the area current passes through, dn/dx and dp/dx terms are the number of electrons and holes with respect to x coordinate. Dn and Dp are the electron and hole diffusion coefficients and expressed as follows[13],

$$D = \frac{kT\mu}{q} \qquad \textbf{(Eq.54)}$$

where k is the boltzman constant, T is the temperature, q is the unit charge and the μ is the mobility of the carriers in the semiconductor.

2.2.6.3. Drift Current

In case of an existing electric field in the semiconductor, the random motion of carriers are affected and modified by this field. The polarization of the carriers result in a net movement of electrons opposite to the direction of the electric field where the holes move in the same direction with the field. This net movement of carriers because of the field is named as drift current. Drift current is affected by the mobility which is a material dependent constant. Also the current is proportional with the charge density and electric field strength. Current density which is the current divided by the area it passes, can be expressed as follows where q expresses the electron charge, n and p electron hole concentrations μn and μp - electron and hole mobilities and *Ex* is the applied electric field[13],

$$J_x = q(n\mu_n + p\mu_p)E_x \qquad \textbf{(Eq.55)}$$

So the current can be also expressed as follows which is the multiplication of the current density with the area[13],

$$I_{Drift} = qA(n\mu_n + p\mu_p)E_x \qquad \textbf{(Eq.56)}$$

2.2.6.4.P-N Junction Operation

When we form a contact between p-type and n-type doped materials, large carrier density gradients arise at the junction. Because of these density differences, electrons diffuse from n to p doped regions, whereas the holes diffuse from p to n doped regions of the materials. These diffusing carriers leave behind uncompensated immobile ionized impurity atoms which forms the region called depletion region. An electric field is formed between the positive ion cores at the n-type depleted region and negative ion cores at the p-type depleted region and due to this electric field a potential called "built-in potential" is formed at the junction and formulized as follows[13],

$$V_{bi} = \frac{kT}{q} \ln \frac{N_A N_D}{n_i^2} \qquad (Eq.57)$$

where N_A, N_D are the p-type and n-type doping densities and n_i is the intrinsic carrier concentration.

In Figure 2.10 the side vision of a PN junction is shown. The depletion region is shown with yellow and the ionized immobile ions can be observed. Finally, on the graph under the junction the built-in potential can be observed. In a p-n junction in case of steady state conditions with no bias, the drift and diffusion currents balance each other.

The electric field at the depletion region is used to separate the generated carriers in a solar cell. In Figure 2.11, the band diagram of a p-type bulk doped with n-type dopants can be seen. Electric field at the depletion region pushes electrons to the n side and holes to the p side of the structure. The E_B shown on the same figure is the potential difference between the oppositely doped sides and prevents the carriers to cross to the other side of the structure.

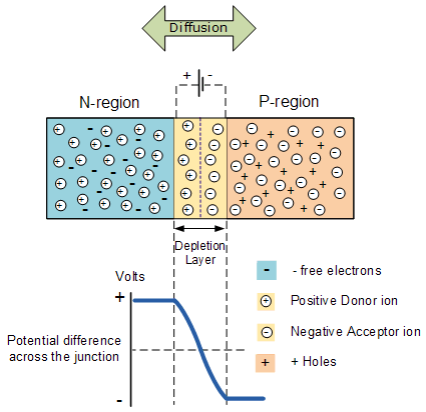

Figure 2.10: Depletion Region and Built-in Potential Visualization on a PN Junction Diagram [6]

The concentration of minority carriers is the limiting factor for the recombination and the increase of the minority carriers in a semiconductor increases the recombination rate significantly, so the separation of carriers is necessary and the most important operation for a solar cell.

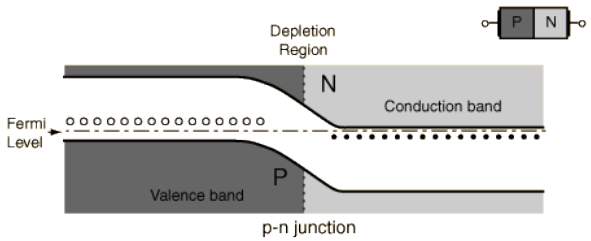

Figure 2.11: Band diagram of a p-n junction[42]

CHAPTER 3

SILVACO TCAD SIMULATOR

3.1. Introduction

Because of the importance of modelling in solar cell development, various simulation tools have been developed and used to understand the behavior of solar cell devices for different inputs. With the help of these tools, the time consumption with trials and errors in the production site and thus expenditure can be reduced significantly. For this purpose the Si Valley Company (Silvaco) has developed the technology computer aided design (TCAD) software Athena and Atlas that are the used to model the processes and device electronics, respectively.

Both ATLAS and ATHENA run in DECKBUILD environment and extensively realistic structure definitions and electrical simulations are performed using this environment.

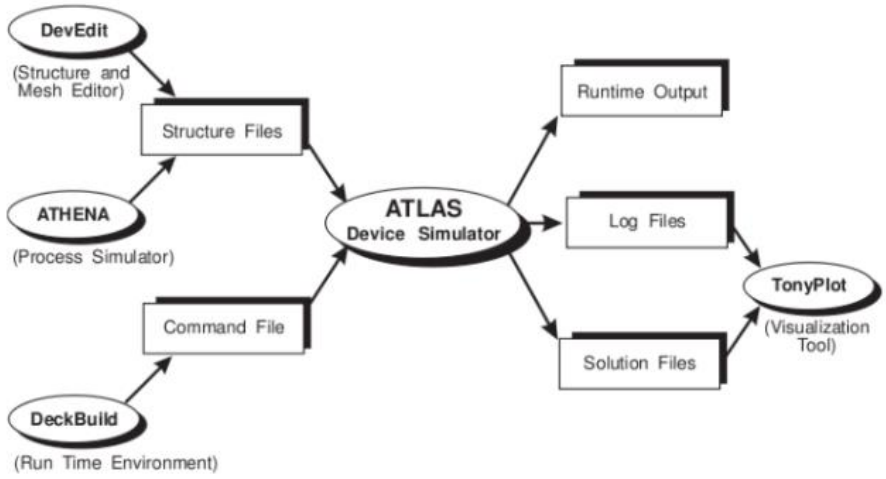

Figure 3.1: Silvaco TCAD Modules

The structure of the device can be defined with the ATHENA module and be transferred to ATLAS module for electrical simulations in the form of structure files or it can be directly designed in the ATLAS module without process simulations. According to the code written in the DECKBUILD the results are stored in to the log and data files to be viewed later on or during the simulation using another module called TONYPLOT. The general input and output visualization of the TCAD is shown in Figure3.1. Another module DEVEDIT can also be seen in the same figure that is a supportive module for mesh definitions.

In this thesis the structure of a solar cell is defined by ATHENA, simulating the process steps at the same time, the optical simulation was not performed with Silvaco but the generation profile is taken from the OPAL 2 web based simulator and the electrical simulation combining the structure and the optical generation profile is conducted with ATLAS module of Silvaco TCAD.

3.2. Structure Specification with Athena

The definition of the structure is required for the simulations either by using ATLAS directly or by including the process details and simulations using the ATHENA module of the Silvaco TCAD. In this thesis, process simulations are also included and the structure definition is performed with the ATHENA module[31].

For defining the structure, first the mesh is arranged, then the materials are set and doping processes are done. Finally, contacts are deposited, passivation layers are included and structure is saved into a structure file to be used by ATLAS later on in the electrical simulations.

Simulations of two-dimensional solar cells are performed in this thesis. Smallest possible structure with the same properties as the whole cell is taken which is called as pitch and divided into many pieces for solving the solutions in each of them. Dividing this structure more than required, causes long solution times whereas weak meshes causes a decrease in the accuracy of results. In Figure 3.2, the structure produced by ATHENA process simulator can be observed. The depth of the cell is

200 µm however only the last 2.4 µm of the cell is shown in figure to show the doping details clearly. Since the optical simulations are studied with OPAL 2 and the generation profile is embedded to the structure, the front side of the cell is not designed in detail with ATHENA. The width of the cell can be observed as 2 mm which corresponds to the sum of 1 BSF, 1 Emitter and 2 Gap regions which equals to two pitch size of a solar cell.

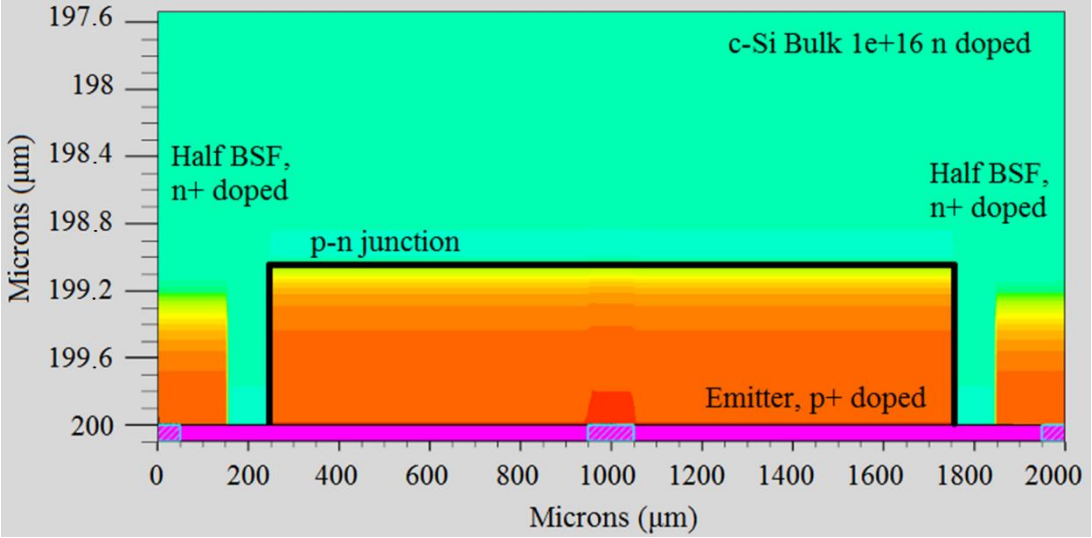

Figure 3.2: Solar cell structure studied by ATHENA

3.2.1. Mesh

Meshing of the structure focused on the surfaces where the dopants are added and detailed analysis is needed. The mesh depth is very small at the edges of the cell whereas it enlarges up to 10 µm or higher at the middle regions of the bulk. In addition, since the gap and contacts are critical the widths of the meshes at these points are as low as 5 µm where in the mid regions of emitter the width can be taken as 40 µm. Much smaller meshes are also tried and it is observed that these values are small enough for precise results.

In Figure3.3, the mesh details of the simulated solar cell structure is shown. Different from Figure, the 200-µm depth of the cell can be observed in Figure and the meshing details of the whole structure can be observed. Top of the figure corresponds

to the front side of the cell where the light comes from; on the other hand the bottom part of the figure is the rear side of the cell where the dopings and contacts are located. It can be observed that the mesh becomes much dense at the sides of the cell. Especially the front and rear sides of the cell and the contact, gap regions are filled with large number of meshes to be analyzed precisely.

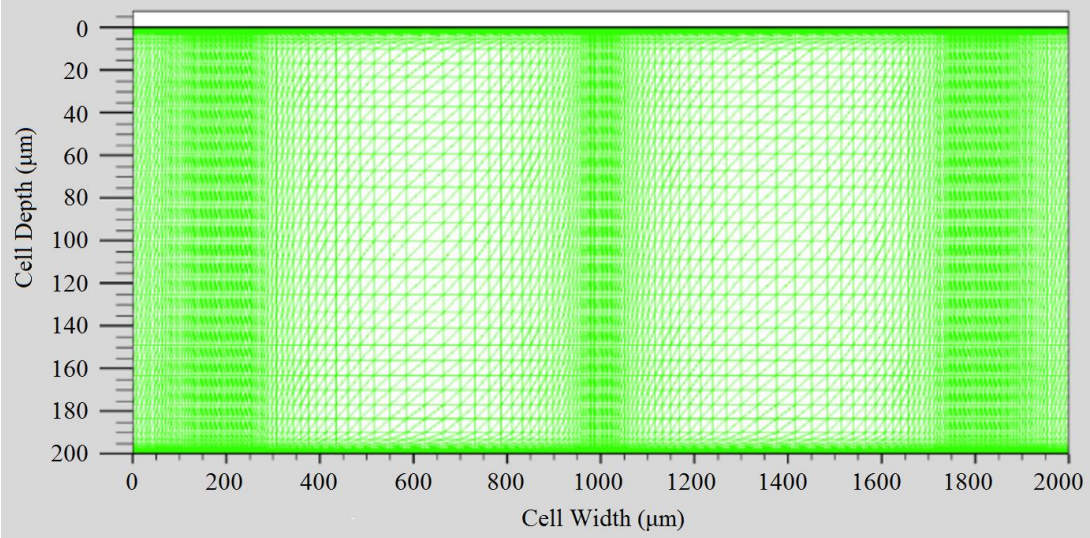

Figure 3.3: Mesh visualization of the solar cell structure

The structure given in Figure 3.3 is produced with the following set of statements written in the beginning of the simulation deck.

The general format of meshes in the DECKBUILD under the ATHENA module is as follows for X-axis:

LINE X LOCATION=<VALUE> SPACING=<VALUES>

and for Y-axis:

LINE Y LOCATION=<VALUE> SPACING=<VALUES>

For X axis the mesh at the sides of the cell starts from 10 µm gets smaller in the gap down to 5 µm than enlarges again and reaches 40 µm in the middle regions of emitter and decreases to 5 µm again at the emitter contact, then continues symmetrically at the other half of the structure. Example of mesh settings is as follows,

```
LINE X      LOCATION =0.00          SPACING=10
LINE X      LOCATION =$wcell/2      SPACING=40
LINE X      LOCATION =$wcell        SPACING=10
```

where full code is given at Appendix A.

In these statements, it is possible to give the values numerically or we can predefine some parameters to be used later on through the deck with a reference. Here some predefined parameters are used while defining the locations of some mesh values, for example: “wbase” refers to width of back surface field region where “wemit” gives the value of emitter width, “wgap” gives the value of gap width and “wcell” gives the sum of these parameters which concludes in the width of the pitch of the cell. These parameters are defined before the meshes just after running the module with “GO” statement as follows.

```
SET    wemit = 1500
SET    wgap  = 100
SET    wbase = 300
SET    wcell = $wemit+2*$wgap+$wbase
SET    depth = 200
```

On the other side if we consider Y axis, it can be observed that the mesh is as small as 40 nanometers at the front and back surfaces where the regions are doped and critical for the simulation. Approaching to the mid regions the mesh enlarges up to 10 μm gradually to decrease the simulation time, since middle parts of the cell is bulk only and no detailed analysis are required. Detailed code is given at Appendix A.

```
LINE Y      LOCATION=0.00           SPACING =0.05
LINE Y      LOCATION=$depth         SPACING =0.04
```

At this point the mesh definitions are complete through the whole cell and the mesh data for the structure on Figure and Figure is complete. Next step is the definition of the material (c-Si) and the doping profiles of the structure.

In Figure 3.4 the back structure of IBC cell which is the model of the cell produced in GUNAM can be observed. The dense mesh profiles at the doped and

contacted regions and rare meshes at the middle regions can be observed. Figure 3.4(a) shows a closer view of the emitter region at the middle of Figure 3.4(b).

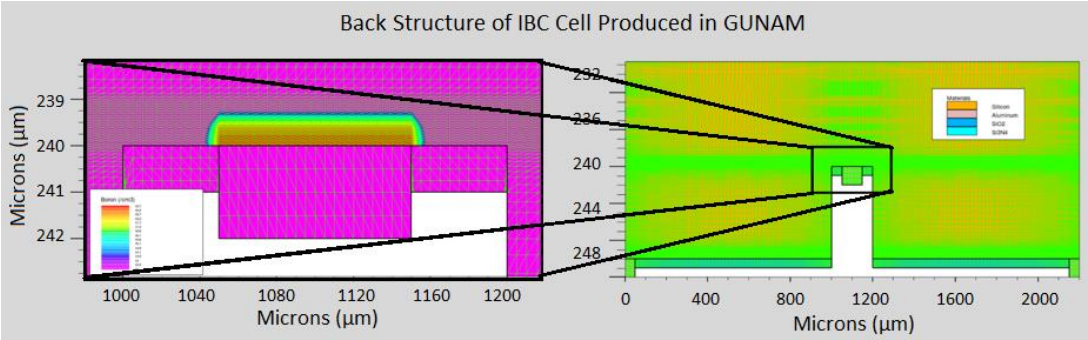

Figure 3.4: Model of IBC cell produced in GUNAM facilities

3.2.2. Material and Doping

As the boundaries of the material are determined, the materials in the structure should be set. Si for the bulk is determined with the following statement indicating that the 2D Si have an initial phosphorus doping of $1x10^{15}$ and the top orientation of the Si is <100>

INIT SILICON C.PHOS=1e15 ORIENTATION=100 TWO.D

After having the bulk silicon, the dopings should be arranged. Since we are using ATHENA module we determine the dopings with processes so first masking should take place that is performed with the following statement for Back Surface Field Region masking.

DEPOSIT OXIDE THICKNESS=0.5 DIVISION=4

ETCH OXIDE RIGHT P1.X=$wbase/2+2*$wgap+$wemit

ETCH OXIDE LEFT P1.X=$wbase/2

At that point, we have an oxide layer that has openings at the right edge and left edge of the back structure so that when doping process is defined the dopants will diffuse to these regions only to form BSF doping which is the following statement.

DIFFUSE TIME=1 hour TEMPRATURE=1000 C.PHOS = $dopingbsf

ETCH OXIDE

With this statement the BSF region has exposed with the phosphorus dopants with the amount determined by “dopingbsf” statement at the beginning of the DECK, for 1 hour at the temperature of 1000 degrees. Finally we etch the masking oxide so that we have the BSF region ready. Same way the Emitter doping and FSF doping are placed and the deck is shown in detail in the Appendix.

3.2.3. Contacts

After setting the structure and placing the dopants, the next step is to deposit the contacts and define them as Electrodes. It is an easy step with another deposit statement and following aluminum etching steps as follows.

```
DEPOSIT ALUMINUM        THICKNESS =0.1     DIVISION=4

ETCH ALUMINUM START          X=$metal/2     Y=-$depth-10

ETCH CONT     X=$metal/2                    Y=-$depth

ETCH CONT     X =$wbase/2+$wgap+$wemit/2-$metal/2  Y=-$depth

ETCH DONE     X =$wbase/2+$wgap+$wemit/2-$metal/2  Y=-$depth-10


ETCH ALUMINUM START     X=$wbase/2+$wgap+$wemit/2+$metal/2
Y=-$depth-10

ETCH CONT    X =$wbase/2+$wgap+$wemit/2+$metal/2  Y=-$depth

ETCH CONT    X =$wcell-$metal/2                   Y=-$depth

ETCH DONE    X =$wcell-$metal/2                   Y=-$depth-10
```

This 4 step etching process etches the rectangular area determined by 4 dots given in the 4 different lines and these statements etches the aluminum between the BSF and Emitter regions so that only aluminum contacts are left at the middle points of the BSF and Emitter regions.

```
# Form electrodes
ELECTRODE       NAME=BSF        X=25
ELECTRODE       NAME =BSF       X=$wcell-25
ELECTRODE       NAME =emitter   X=$wbase/2+$wgap+$wemit/2
```

Finally the contacts are defined as electrodes with the names “BSF” and “Emitter” to be used later on by the ATLAS module for arranging and solving currents and voltages. At that point the structure is ready to be simulated electronically. For transferring the structure to the ATLAS module it is saved in to the IBC01_0.str file with the following command.

```
STRUCTURE       OUTF=IBC01_0.str
```

After defining the contacts, final appearance of the back structure of the simulated cell structure is shown in Figure 3.5.

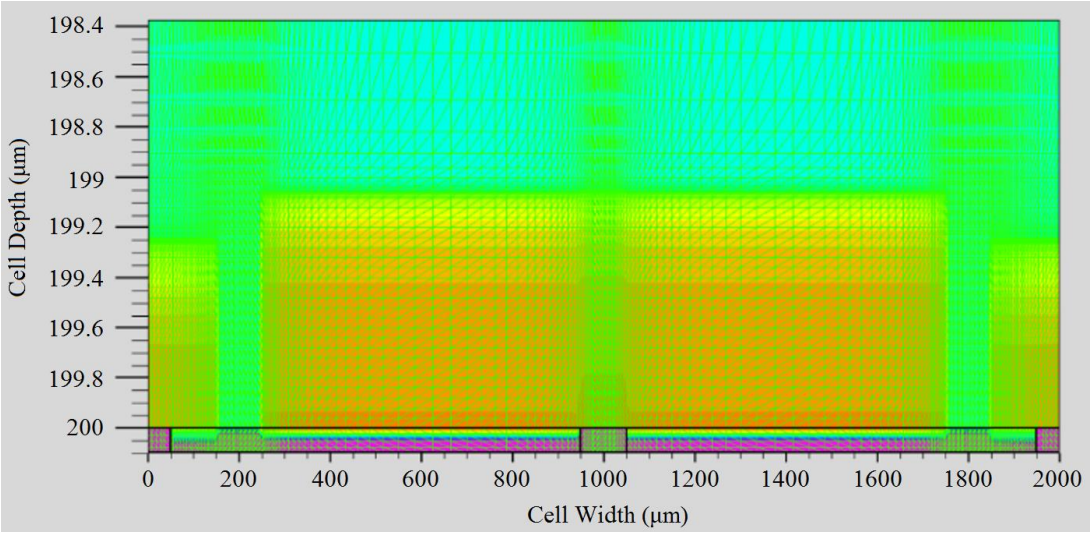

Figure 3.5: Back surface zoomed visualization for observing dense meshes

3.3. Electrical Simulation with Atlas

After building the structure in ATHENA module we start ATLAS module with “GO ATLAS”

command and continue with electrical specifications. If ATLAS module is in the same DECK with ATHENA there is no need for structure specification but if modules are prepared in different DECK's, than an extra file insertion command is needed to specify the structure to be used in the electrical simulations.

3.3.1. Bulk and Surface Recombination Velocities

As the ATLAS module has activated and structure is specified the bulk life time and surface recombination velocities should be identified as follows.

```
MATERIAL    MATERIAL=Silicon TAUN0=1e-3  TAUP0=1e-3
```

With this statement we have identified that the bulk life time for electrons and holes in the Si structure will be 1 millisecond. The unit for tau is taken as second in this statement.

Contact surface recombination velocities are set to $1x10^7$ cm/s which is the carrier saturation velocity in a semiconductor. So we accepted highly conductive and well produced contacts not to limit or disturb our results with contact problems initially. In case of a decrease in the SRV values at contacts, first the minority carriers are effected than with further increase the majority carriers are effected and efficiency decrease is observed, the detailed observations and graphs will be given in the "Results" section of the thesis. The contact SRV values are expressed with following statements:

```
CONTACT     NAME=emitter   SURF.REC VSURFN=10000000
VSURFP=10000000

CONTACT     NAME =base     SURF.REC VSURFN=10000000
VSURFP=10000000
```

Following the contact SRV values, the interfaces of Emitter, BSF, FSF and gap are defined with the statements below

```
INTERFACE          X.MIN=0       X.MAX=20000       Y.MIN=-5
Y.MAX =5           S.N =5000 S.P=5000   S.I
```

The first statement sets the SRV value of front surface field region. The interface between -5 and 5 μm which is the front interface is given the SRV values of 5000 for both electrons and holes. SRV values for doped region is taken as 5000 initially [32], since the minority carriers are very small in numbers at the edges because of the doping, the SRV values should be taken in the range of thousands.

INTERFACE X.MIN=0 X.MAX=$wbase/2 Y.MIN=80 Y.MAX =300 S.N =5000 S.P=5000 S.I

INTERFACE X.MIN =$wbase/2+$wgap X.MAX =$wbase/2+$wgap+$wemit Y.MIN =80 Y.MAX =300 S.N =5000 S.P=5000 S.I

INTERFACE X.MIN =$wcell-$wbase/2 X.MAX =$wcell Y.MIN =80 Y.MAX =300 S.N =5000 S.P=5000 S.I

INTERFACE X.MIN =$wbase/2 X.MAX =$wbase/2+$wgap Y.MIN =80 Y.MAX =300 S.N =30 S.P=30 S.I

INTERFACE X.MIN=$wbase/2+$wgap+$wemit X.MAX=$wbase/2+$wgap+ $wemit+$wgap Y.MIN =80 Y.MAX =300 S.N=30 S.P=30 S.I

These 5 interface statements sets the SRV values of BSF on the left, Emitter, BSF on the right, 1st Gap and 2nd Gap respectively. These regions can be observed in Figure 3.6.

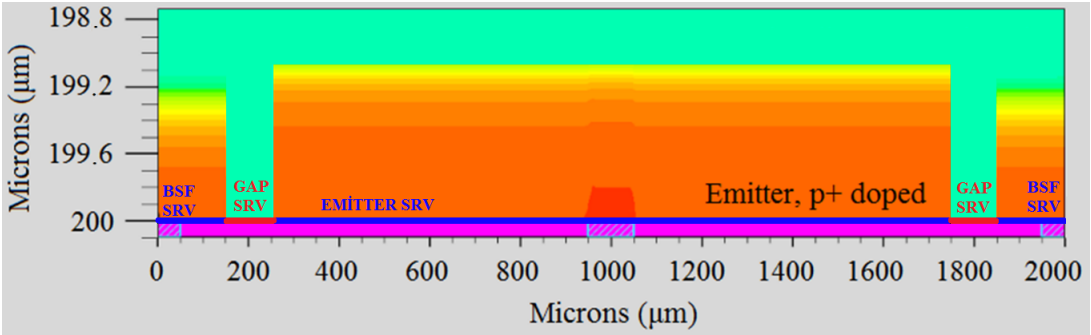

Figure 3.6: Illustration showing SRV regions on a solar cell schematic

Since there is no doping at the gap regions the SRV value is set to 30 representing a well passivated non-doped region[32]. On the other side for BSF and Emitter regions the SRV value is taken as 5000 cm/s again representing a well passivated but doped region for the non-contacted parts.

3.3.2. Importing Generation Profile

Next statement defines the generation profile of the structure. The profile is extracted from the OPAL 2 [24] web based optical simulator which gives approximate but not exact generation profiles. This profile is satisfactory for our study since it approaches the real values and will be used through all sets of simulations where it does not change significant values throughout the study. The data is extracted from the website and converted into a data file that can be read by the Silvaco TCAD tool. Then with the following statement it is saved as the generation profile and named as the beam number 1 to be later on used at the solution section.

```
DATASET     INFILE=200UmgentextureWRT.log          NAME=photo
ABS.CHAR    AXIS.YXZ    FY1=0 FY2=200 TY1=0 TY2=200

BEAM  NUMBER=1 CHARACTER=photo
```

3.3.3. Electrical Models

The simulation tool Silvaco TCAD uses basic semiconductor equations given in section 2.2.1 by default. Poisson's equation, Carrier Continuity equations, Transport equations which all of them are explained in detail in the same section are included in all semiconductor simulations and are derived from Maxwell's laws.

The specification of the models is the last step, before the solution of the system. The following statement selects the models to be used while the solutions are being performed.

```
MODELS      klamob srh auger fermi print
```

Each model specifies the following properties and solution details,

Klamob: Klaassen Mobility model accounts for a broader set of effects and has been calibrated over a wider range of conditions than any other low-field bulk mobility models. It relates the low-mobility to donor, acceptor, lattice, carrier-carrier scattering, and temperature.

The total mobility can be described by its components as follows[25];

$$\boldsymbol{\mu_{n0}^{-1} = \mu_{nL}^{-1} + \mu_{nDAP}^{-1}} \qquad \textbf{(}\boldsymbol{Eq}\textbf{.58)}$$

where μ_{nL} is the lattice scattering component and μ_{nDAP} is the impurity-carrier scattering component it is the electron mobility due to Donor (D), acceptor (A), screening(P) and carrier-carrier scattering[25],

$$\boldsymbol{\mu_{nL} = 1417 * (\frac{300}{T_L})^{2.285}} \qquad \textbf{(}\boldsymbol{Eq}\textbf{.59)}$$

$$\boldsymbol{\mu_{nDAP} = \mu_{N,n} \frac{N_{nsc}}{N_{nsc,eff}} (\frac{9.68x10^{16}}{N_{nsc}})^{0.68} + \mu_{pc} (\frac{n+p}{N_{psc,eff}})} \qquad \textbf{(Eq.60)}$$

where $\mu_{N,n}$ is the impurity scattering component and μ_pc is the carrier-carrier scattering component

Srh: Presence of traps (defect) within the forbidden gap provides phonon transitions. This transition is explained and derived by Shockley and Read first and then by Hall. The recombination called as Shockley-Read-Hall recombination and modelled as follows[25],

$$\boldsymbol{R_{SRH} = \frac{pn - n_{ie}^2}{\tau_p[n + n_{ie}] + \tau_n[p + n_{ie}]}} \qquad \textbf{(}\boldsymbol{Eq}\textbf{.61)}$$

where τ_n and τ_p are electron and hole lifetimes with constant values used for the corresponding simulation

Auger: Auger recombination requires three particles for the transition. A mobile carrier is captured or emitted during the transition. Auger recombination is activated during the studies in this theses and modelled as follows[25],

$$R_{Auger} = 2.8x10^{-31}\left(pn^2 - nn_{ie}^2\right) + 9.9x10^{-32}(np^2 - pn_{ie}^2) \quad \textbf{(Eq.62)}$$

Fermi: With Fermi statement the Fermi-Dirac and Boltzmann carrier statistics mentioned above in section 2.2.2.1 are used in the calculations and all of them are explained in detail at the referenced section.

Print: The status of models and a variety of constants and coefficients are printed to the output deck for observation.

3.3.4. Solution

After specifying the structure and electrical properties the system requires a file to save the results and this file is specified as follows:

LOG outfile=IBC01_01.log

So the results of the solutions done after this statement will be stored in the "IBC01_01.log" file for later observations.

Following this statement, solution of the system starts with the following initial solution statement,

SOLVE INIT

Continues by the addition of the generation profile with the following statement,

SOLVE B1=1.0

and the final step is the voltage sweep at the emitter contact of the solar cell which will produce the current values for each voltage value between the range of 0V to 0.76V with a step of 0.02V. The statement for this command is as follows,

SOLVE NAME=emitter VBASE=0.0 VSTEP=0.02 VFINAL=0.76

With this command the solution of the system is completed and the results are stored in the specified LOG file. A structure file is also needed to store the structure with the solved electrical data to visualize later on with the vision of structure. The following statement stores the structure data in to the “IBC01_02.str” file.

```
STRUCTURE          OUTF=IBC01_02.str
```

3.4. Results

For analyzing the results the TONYPLOT module is used as it is mentioned in the “Introduction” part. To open the pre-saved data in the “IBC01_01.log”, “IBC01_02.str” files following simple statements are needed,

```
TONYPLOT    IBC01_01.log

TONYPLOT    IBC01_02.str
```

The I-V curves are extracted from the log file and the structure with its electrical properties can be observed with the structure file. These analysis are made using the user-interface of the TONYPLOT module which allows any kind of display capabilities with many modifications on the graph. The graphs given in the results part of the thesis are extracted through this interface.

There are also some other ways for solving solar cell which is the following simple statement that extracts the I-V curve of the structure directly but the sweep to be performed is given by myself in my simulations.

```
SOLAR          IV="Voc,Jsc,Pmax,FF”
```

Another way of extraction of results is the “Extract” statement which directly prints out the required data from the file to the output deck. The Following set of statements includes the log file prepared before and extracts the following data respectively:

Current, power curve, maximum power, voltage and current at maximum power point, current density in mA/cm^2, open circuit voltage, fill factor, efficiency and I-V curve.

```
EXTRACT INIT INFILE="IBC01_01.log"

EXTRACT NAME="Jsc" Y.VAL FROM CURVE(v."emitter", i."base") WHERE X.VAL =0.001

EXTRACT NAME ="P" CURVE(v."emitter", (v."emitter" * i."base")) OUTF="solarex12_P.dat"

EXTRACT NAME="Pm"MAX(CURVE(v."emitter",(v."emitter" *i."base")))

EXTRACT NAME ="Vm" X.VAL FROM CURVE(v."emitter", (v."emitter" * i."base") ) WHERE Y.VAL =$"Pm"

EXTRACT NAME ="Im" $"Pm"/$"Vm"

EXTRACT NAME ="JscmAcm2" $Jsc*1e08*1e03/$wcell

EXTRACT NAME ="Voc" X.VAL FROM CURVE(v."emitter", i."base") WHERE Y.VAL=0.0

EXTRACT NAME ="FF" $"Pm"/($"Jsc"*$"Voc")*100

EXTRACT NAME ="Eff" ($Pm*1e08/(0.100037*$wcell))*100

EXTRACT NAME ="IV" CURVE(v."emitter", i."base") OUTF="STRUCTURE OUTF=IBC01_02.dat"
```

CHAPTER 4

SIMULATION RESULTS

All details of the deck used for the IBC simulations are given in the 3rd chapter and the code can be found at the appendix as one piece. The code given, forms the basis of the study presented in this chapter. However before extracting the results of IBC structure the consistency of the program has been controlled and Schockley Queisser limits have been tested with details given in the chapter 4.1. Following the test procedures of the program the IBC simulations are performed. The optical simulations are given at chapter 4.2 and the electrical simulations and results are presented at chapter 4.3 in detail.

The study started with selection of realistic bulk life time and bulk doping values, optimization of these values and visualization of unrealistic cases about these parameters. It has continued with emitter fraction and dimension optimizations of the structure. Different optimized final structures are set for different bulk doping values. Emitter and BSF widths and fractions are optimized and the IBC structure which has been used in Bifacial IBC cell study, presented in Chapter 5, is determined.

4.1.Schockley Queisser Limit

Schockley Queisser limit is the maximum theoretical efficiency limit of a solar cell with a single p-n junction. The efficiency can be maximized with a semiconductor having a bandgap of 1.34 eV and the limit efficiency of 33.7% can be reached with this semiconductor, according to the Schockley Queisser limitations. Si which is the most common material for solar cell production have a bandgap of 1.1eV which can be improved up to 29.4% efficiency theoretically.

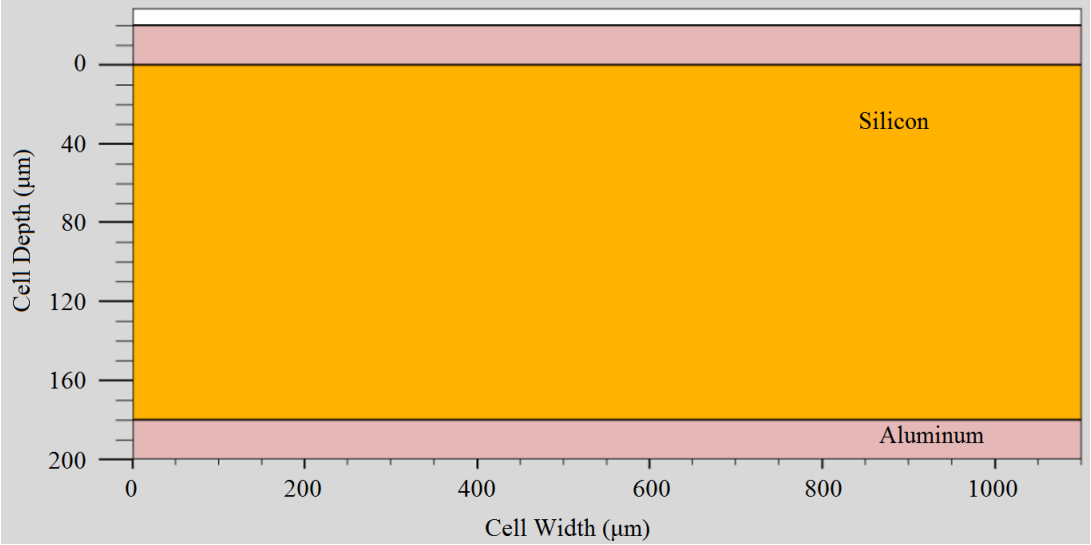

Figure 4.1: Simple solar cell structure for the highest efficiency

For the consistency of our simulation tool, first this limit efficiency is tried to be reached by cancelling all loses. All recombinations are cancelled other than Auger recombinaton, bulk life time and surface recombination velocities are arranged as given in the following table and full spectrum generation is assumed and inserted in to the cell without an optical simulation. Both sides are metallized and a very simple diode structure with a wide range of doping profiles is used. In Figure 4.1, the simple structure can be seen.

The simulations are performed for cells with different bulk lifetimes and with different emitter doping profiles. The resultant efficiency values are between the values 29,4-29.6% for different cases, which is an acceptable and small difference for wide range of profiles and junction depths. Some of the results are shown in Figure 4.2. It is also observed that the cell size does not have an effect on the result for the perfect condition case. As a result, for perfect cell reaching the Schockley Queisser limitations, the signifacant cell parameter changes do not effect the results signifacantly since the upper limit has already been reached.

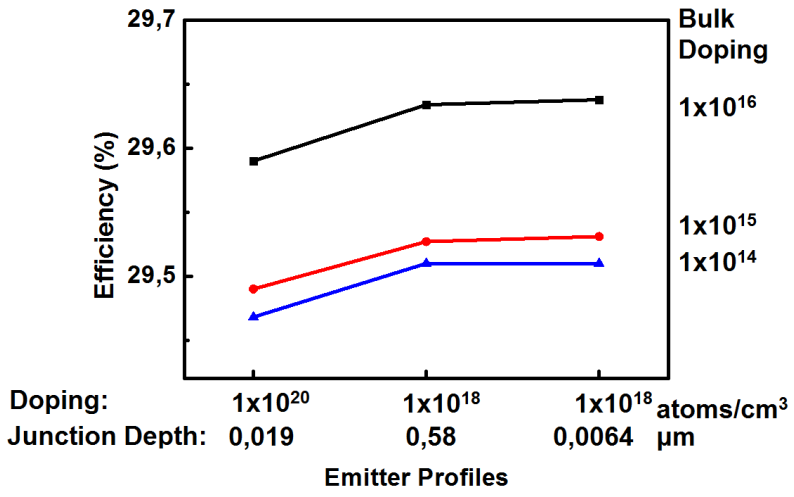

Figure 4.2: Efficiency saturation at Shockley-Queisser limit with different cell parameters

4.2.Optical Simulations with OPAL 2

Optical simulations were not performed in an advanced level in this thesis but it is included to obtain the electrical simulations in a more realistic manner. Simple simulations using the OPAL 2 [24] optical simulator of the PV Lighthouse website is used to obtain the reflection, absorption and transmission data as well as the generation profile in the Si structure with respect to its depth.

200 µm thick crystalline Si bulk with a simple textured front surface having upright pyramids coated with 79 nanometer Si nitride is simulated. The anti-reflection coating thickness is also optimized by the simulator to maximize the absorption in the Si region. Character Angle is taken as 54.74 degrees and AM1.5 initial light is sent to the structure. The details of the OPAL 2 [24] simulator is given in the chapter 2.1.4.

Reflection, absorption, transmission data for the ARC film deposited to the front side is obtained and is shown in Figure 4.3, here the transmission portion will be accepted as the absorbed light in the Si substrate. Numerically the input light is given

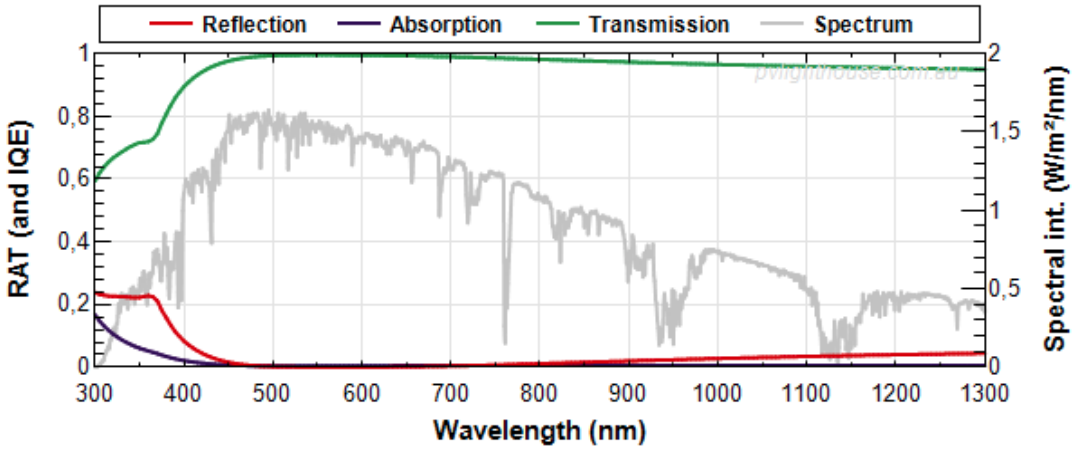

Figure 4.3: Reflection and absorption data of textured, ARC coated solar cell structure

such that the current density of the structure corresponds to 44,10 mA/cm^2 in for 100% transmission, where according to the simulations the 97,4% of this input light is absorbed in the Si, which corresponds to 42,95 mA/cm^2 of output current density from the cell. Lost current density portion of 0,83 mA/cm^2 is reflected from the front surface and the remaining 0,33 mA/cm^2 is absorbed in the front films. For this simulation the back stage losses are neglected.

4.3.Electrical Simulations with Silvaco TCAD

4.3.1. Process Simulation with Athena

Silvaco gives user the opportunity to define the initial structure with Athena by including process details as well as with Atlas in a much simpler way without any process concerns. Same structure can be defined both ways but, by using Athena, modelling the exact processes in the lab is possible which also gives a final structure which is much closer to the real one. By using the Athena module of Silvaco TCAD, doping optimizations can be performed and structure that is much more realistic is defined for future electrical simulations. A simple doping process is developed which suggests only one drive-in step for both phosphorus and boron dopings of the structure.

4.3.2. Simulated IBC Solar Cell Structure

Following the optimizations of the doping processes, a default structure for the optimization of the IBC cell is defined. Initial dimensions of emitter width between 1000-2000 μm and back surface field in the range of several hundred microns are used with an approximate emitter coverage of 70% considering some published papers [33][34]. After initial optimizations, the default structure is set with an emitter width of 1500 μm and BSF width of 300 μm with a 100 μm gap between them. These parameters are set with the consideration of some production limitations in GUNAM facilities, on the other hand it is observed that much smaller and dense structures can give much higher efficiency results.

The doping profiles are also given a default initial value to be optimized later on for this specific structure. Bulk doping density is set as $1x10^{16}$ atoms/cm^3 (i.e. doping density typically used in GUNAM). Peak doping density at emitter and BSF regions are taken as $1x10^{20}$ atoms/cm^3 whereas it is taken as $1x10^{19}$ atoms/cm^3 for FSF region. These doping profiles are produced with process simulations in ATHENA module. Diffusion of dopants occurs under 1000 degrees for 1 hour and profiles fitting an error function have been obtained with an approximate depth of 1 μm for emitter and 0.8 μm for BSF region.

Metals are chosen as small as possible which is 100 μm and the non-contacted regions are passivated with oxide. Metal width and SRV optimizations also take place after emitter and BSF structure is set.

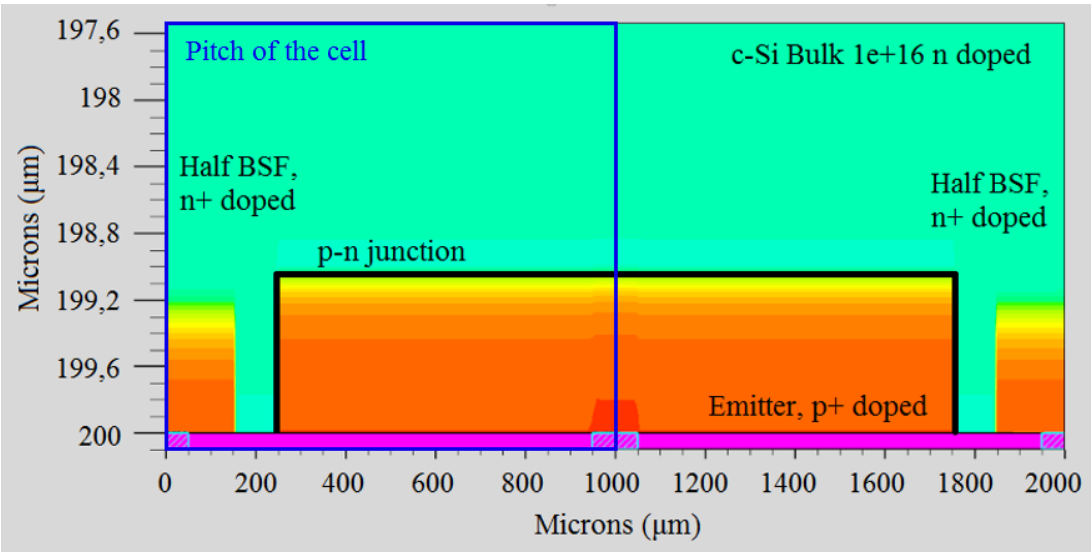

Figure 4.4: Back Structure of the IBC solar cell

A default structure is produced with the parameters given and the visual details of the rear side can be observed in Figure 4.4. Emitter is placed in to the middle where half of the BSF exists at the 2 sides of the structure. Two gap region between emitter and BSF can also be seen easily in the figure. Emitter metal at the middle and half BSF metals at the sides with 100-µm width per region can also be seen in the structure with the dashed lines. Non-dashed pink regions are the non-metal covered regions which are passivated with an oxide layer.

Another input data for the simulation was the SRV values. For doped regions 5000 cm/s is used as the SRV values initially according to published data[32]. Since there is very small number of minority carriers at the outer interfaces of doped regions, only such large number of SRV values corresponds to 50-100 cm/s effective recombination velocities. For Gap region, SRV value is taken as 30 cm/s representing a well passivated gap region. Finally the bulk life time of Si is set as 1 ms and the simulations performed with this default structure.

4.3.3. Bulk Doping and Bulk Life Time Relation

The bulk life time of a semiconductor is limited by its doping because each dopant atom in the semiconductor behaves like a trap for electrons and holes resulting an increase in the recombination rate. The doping amount of the bulk should be chosen to reach the balance, since the higher doping rates decreases the resistivity of the bulk but causes increased recombination rates.

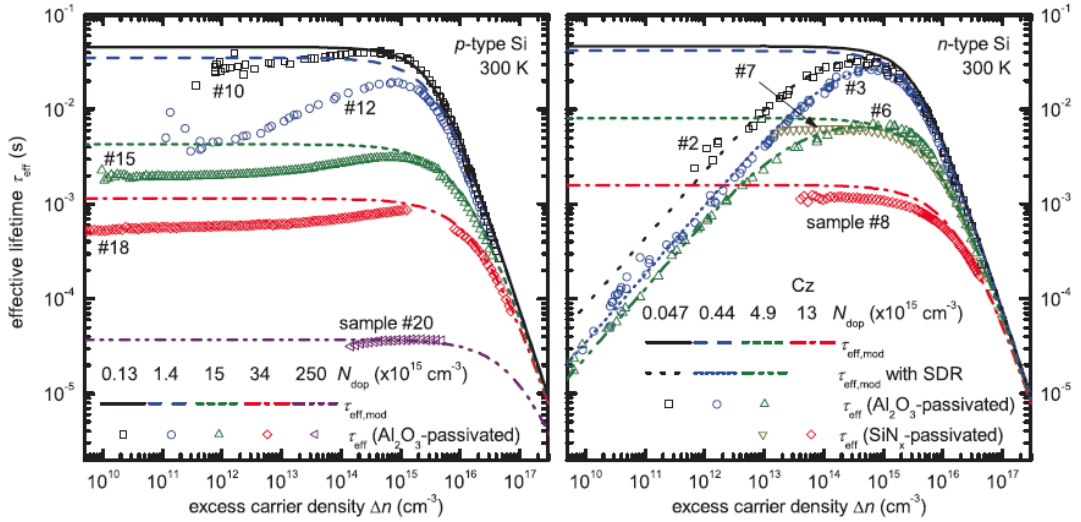

Figure 4.5: Bulk life time vs. excess carrier density for (a) p-type, (b) n-type[29]

In Figure 4.5 [29] the maximum bulk life time values for corresponding excess carrier densities are given for both p-type and n-type bulks. For the same amount of excess carrier densities it is shown that different bulk doping values results in different bulk life time values limiting it from the top.

Decreasing the bulk doping increases the maximum bulk life time value. Following these observations first sweep is done to observe the best choice for the bulk. The default structure defined in the chapter 4.3.2 is utilized for the bulk doping sweep with different bulk life time values. The result is given in Figure 4.6.

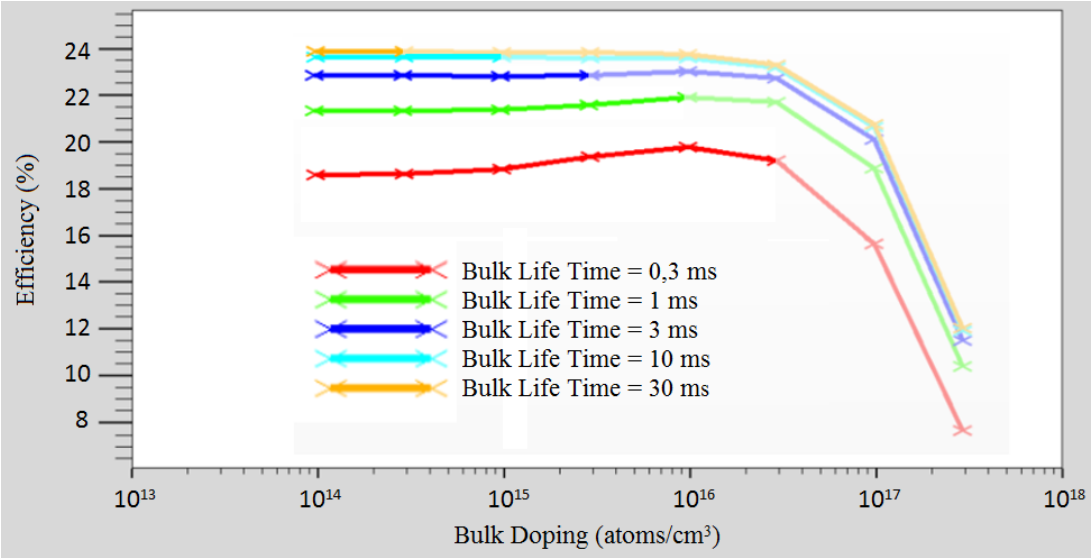

Figure 4.6: Bulk doping sweep

Efficiency increases as the bulk doping increases up to the doping value of $1x10^{16}$ atoms/cm^3. Over that value, the auger recombination dominates and decreases the efficiency significantly. In the same figure, it can also be observed that the efficiency increases as the bulk lifetime increases which is an expected behavior. Figure 4.6 includes some non-realistic data points that have high bulk doping and high bulk lifetime at the same time. In Figure 4.6 it is shown that the doping level of $1x10^{16}$ atoms/cm^3 does not allow lifetime values over 1 ms or the doping level of $1x10^{17}$ atoms/cm^2 does not allow lifetime values over 100 µs approximately. Therefore, these unrealistic data points are shown transparent in Figure and included just to observe the trend of increasing bulk doping and life time at the same time. The closer look without unrealistic data is shown in Figure 4.7.

It is shown that less doped bulks with high lifetimes or highly doped bulks with smaller lifetimes are left when realistic values are plotted. It can be seen that higher bulk lifetime improves the efficiency much faster than highly doping the structure. It seems more logical to choose a high quality Si rather than well doped Si bulk having smaller bulk lifetimes.

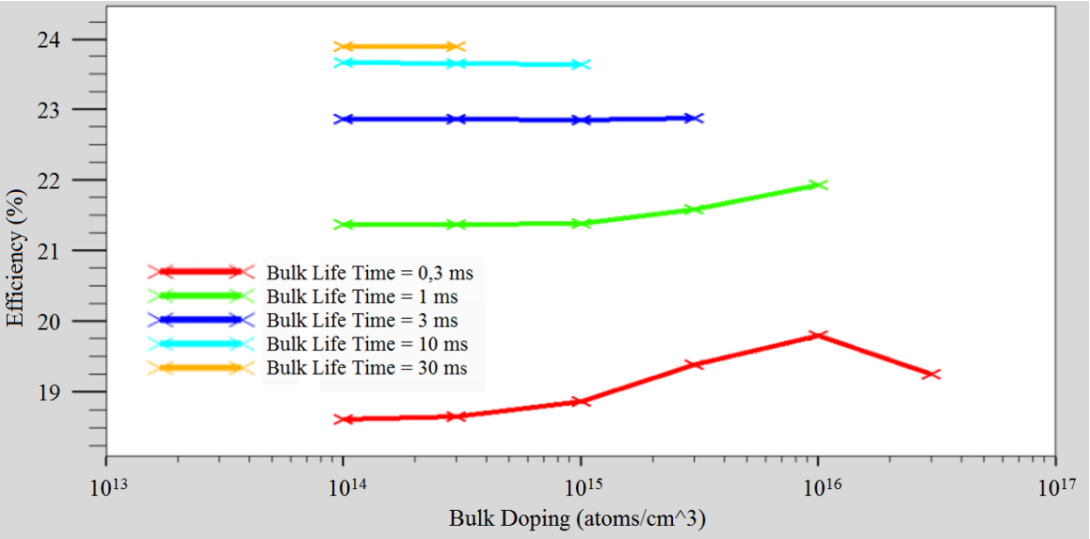

Figure 4.7: Bulk doping sweep (closer look)

The n-type bulks being used for IBC cells in GUNAM facilities are doped with an amount of $1x10^{16}$ atoms/cm^3. First back structure optimization sweeps are done following this information and the bulk doping is kept at $1x10^{16}$ atoms/cm^3. Later on, the less doped bulks having higher lifetimes have also been utilized for comparison.

4.3.4. Emitter Fraction Optimization

First optimization is done to set an optimum emitter and BSF width values which will be used as default values for the following simulations. To observe the optimum emitter fraction in this study an initial pitch size of 2000 µm is set and the emitter width has increased from 900 µm to 1700 µm together with a decrease in the BSF width from 900 µm to 100 µm. Adding 2 gap regions with a width of 100 µm each, the total cell width of 2000 µm remain constant throughout this sweep. The aim of this study was to observe an emitter fraction that gives the highest efficiency. The first data set can be observed in Figure 4.8.

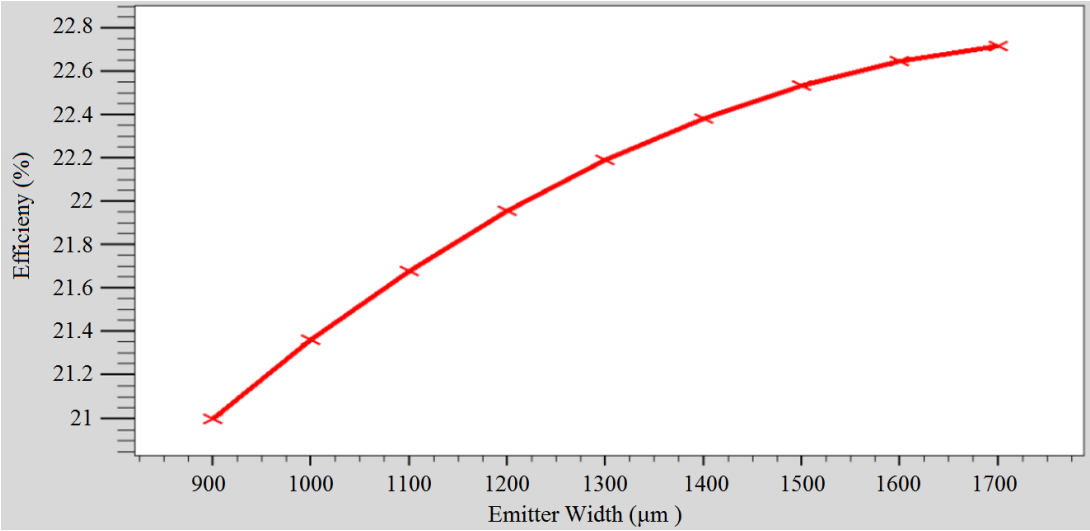

Figure 4.8: Emitter fraction sweep

It is observed that the efficiency increases as the emitter width increases and BSF width decreases. The highest efficiency is obtained for the structure having an emitter of 1700 µm wide and BSF of 100 µm wide. Initial expectation was to observe a peak value around an emitter fraction of 70-80%[35]. To understand this continuous increase in the efficiency, a detailed analysis has been performed in the following two sections by setting either the emitter or BSF width to a constant value while sweeping the other width value to observe the behavior of the efficiency curve with respect to the emitter or BSF width separately.

4.3.5. Emitter Width Optimization

First, constant BSF width values are set and wide range of emitter width values are tried from 100 µm to 3000 µm for 6 different BSF width values from 100 µm to 600 µm. So with this sweep we observed the effect of the Emitter width and BSF width on the efficiency separately, but later on for fixed emitter width values more detailed BSF width sweeps have also been performed.

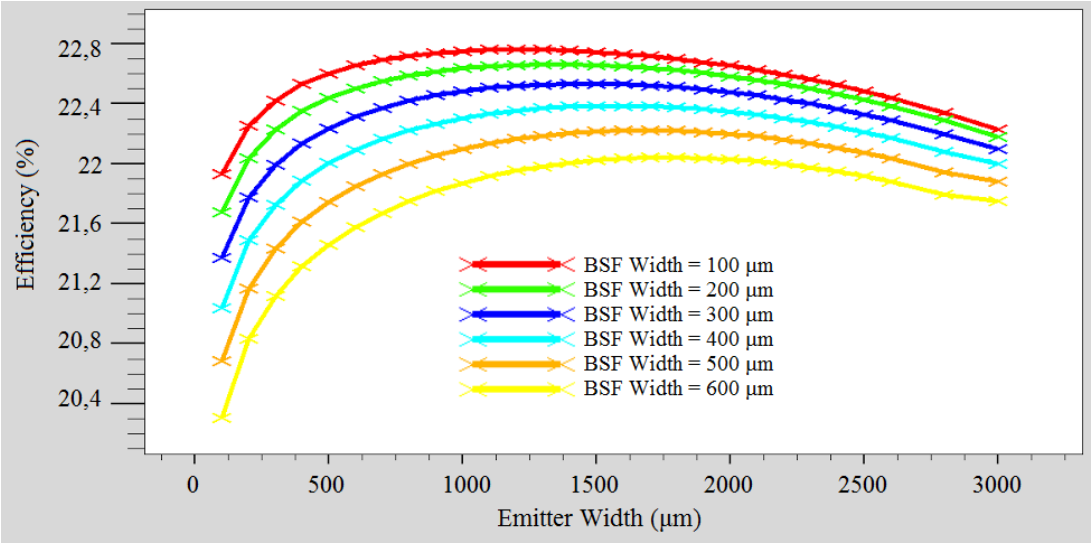

Figure 4.9: Emitter width optimization

Figure 4.9 shows that emitter width has a peak between 1000 µm and 2000 µm for different BSF widths. As the emitter width takes smaller values, the junction gets smaller in the structure and the separation of the carriers weakens, which results in a decrease in the efficiency. This effect is shown on fill factor graph of the same sweep in Figure. On the other hand, as the width of the emitter increases too much, the minority carriers that are generated over the middle of the emitter cannot reach the BSF contacts but they are recombined in the bulk because of the limited bulk lifetime. It is shown that the emitter width sweep for a constant BSF works in consistency with the real expectations. So the explanation of the continuous increase in efficiency with the increased emitter fraction will be explained by the BSF width sweep behavior.

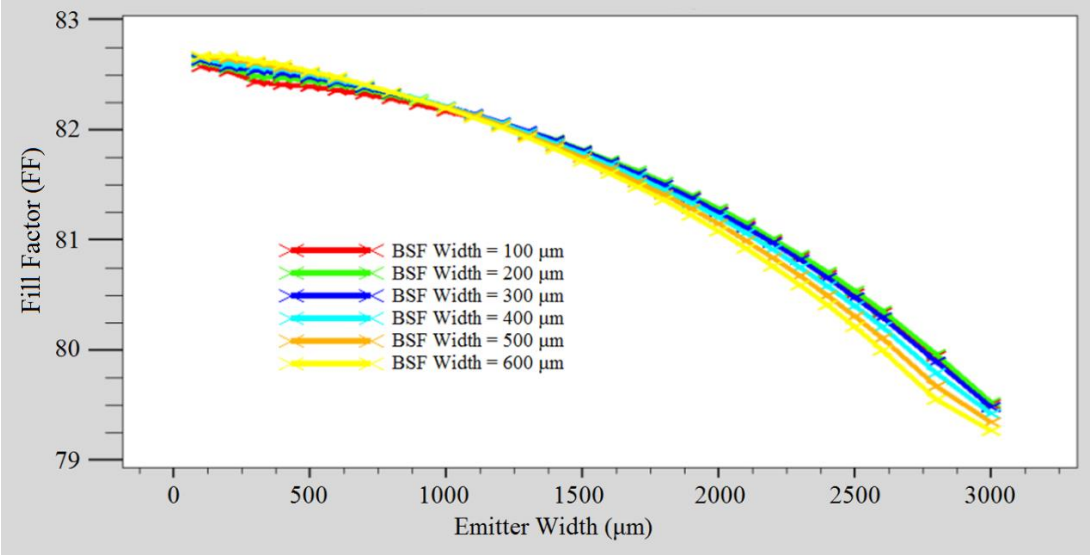

Figure 4.10: Fill factor graph for emitter width optimization

It is shown that the BSF width of 100 µm, which is represented by the red line, gives the highest efficiency for each emitter width value in Figure 4.10 The continuous increase of efficiency with the decreasing BSF width was not the expected outcome of this study. The amount of carrier passing from unit area over the BSF region increases too much when the emitter fraction gets closer 100%. Because same amount of carriers are collected at the emitter and BSF contacts. The power loss at that dense region can be calculated by the following equation.

$$\boldsymbol{Power\ loss = I^2 * R} \qquad \textbf{(}\boldsymbol{Eq}\textbf{.63)}$$

The reason of that behavior is the low resistivity of the bulk having a phosphorus concentration of $1x10^{16}$ atoms/cm^3. The power loss at that region by increasing the carrier density does not become observable because of the low resistance. To observe this power loss effect and to observe the efficiency peak in the emitter fraction sweep the trials with bulks having a concentration of $1x10^{15}$ atoms/cm^3 are also done on the following sections.

How small the BSF width should be chosen, can be determined by process limitations. Considering the limitations in GUNAM facilities the width should be

larger than 200 µm and checking the Figure another simulation sweep is done for BSF optimization for constant emitter widths in the range of 1000 to 1600 µm.

4.3.6. BSF Width Optimization

In Figure 4.11 , the BSF width sweep for the emitter values of 1000, 1100, 1200, 1300, 1400, 1500, 1600 µm can be seen. The increasing behavior in the efficiency through decreasing BSF width can also be seen in this plot. However, the resistive effects which should rise with very small BSF widths, could not be seen in Figure. The reason is the highly doped and conductive bulk which will be studied in the following studies. So the exact optimized values will be determined after the studies with smaller bulk doping but so far considering the Emitter and BSF width optimization studies and the limitations in the facility, the emitter and BSF width values are determined as 1500 and 300 µm, respectively. 300 µm for BSF is chosen for easy production and in Figure 4.11 it is shown that the yellow line which corresponds to 1500 µm of emitter width gives the highest efficiency for BSF width of 300 µm. The cell design for high resistive bulks is simulated next, to observe the peak in the emitter fraction sweep and to have better idea about the efficiency trends with respect to BSF and Emitter width changes.

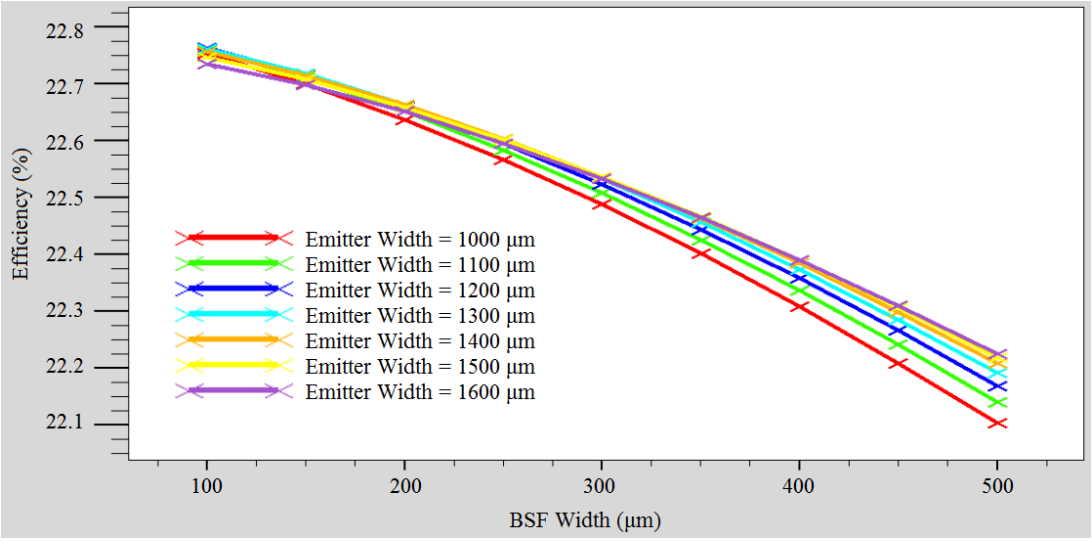

Figure 4.11: BSF width optimization

4.3.7. Emitter Fraction Sweep with Resistive Bulk

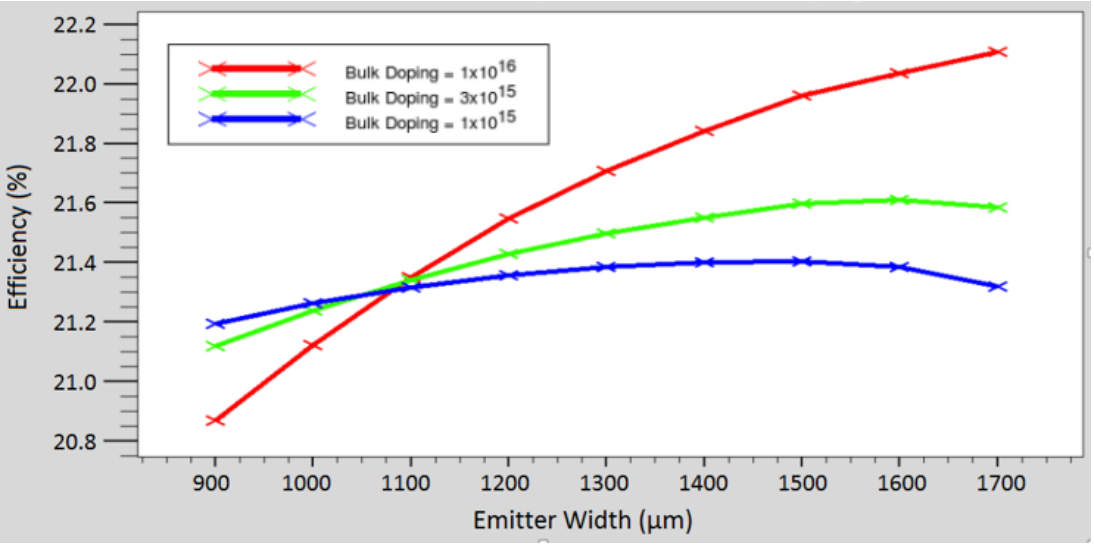

Figure 4.12: Emitter fraction sweep for bulk doping values of $1x10^{16}$, $3x10^{15}$, $1x10^{15}$ atoms/cm^3

After the reason for continuous efficiency increase in the emitter fraction-efficiency graph at chapter 4.3.4 has been understood, the doping level of bulk has been reduced to $3x10^{15}$ and $1x10^{15}$ atoms/cm^3 to observe if the expected peak will be obtained or not. In Figure 4.12 the desired peak is shown easily for decreased bulk doping values. The efficiency peak formation was obtained with an emitter fraction of 79%, which is calculated by the division of emitter width to the sum of emitter, gap and BSF widths. The resistance in the bulk is larger than the previous higher doped bulk which increases the power loss over the BSF region when the BSF width is small.

When the emitter fraction kept increasing over 80%, the loss mechanism over the BSF region becomes more effective than the positive effect of emitter width increase and the efficiency decrease can be observed. Below this value the BSF region is wide enough to accept the incoming carriers without a significant loss. Decreasing the emitter fraction further below 80% results in an efficiency loss since the area of the p-n junction decreases which causes a weak separation in the structure. Approximately 80% of Emitter fraction corresponds to the balance point between the loss mechanism at the BSF region and power of Emitter separation.

4.3.8. Emitter Width Sweep With Bulk Doping Value of 1x10^{15} atoms/cm^3

Both emitter and BSF width sweeps have been performed for two different bulk life time values which are 1 ms and 10 ms. Since the bulk doping has decreased to 1x10^{15} atoms/cm^3, which means the trap states in the bulk has decreased, the maximum bulk life time value has increased as mentioned in detail at chapter 4.3.3. So for comparison the simulations are performed for 2 different bulk life time values.

In Figure, the Emitter width sweep for six different BSF width values can be seen. When compared with Figure 4.13, we can observe that the peak efficiencies have shifted to a smaller emitter width values. The reason is that the bulk is more resistive which means carriers separated, especially at the middle regions of emitter, will lose more energy while traveling to the BSF region of the structure.

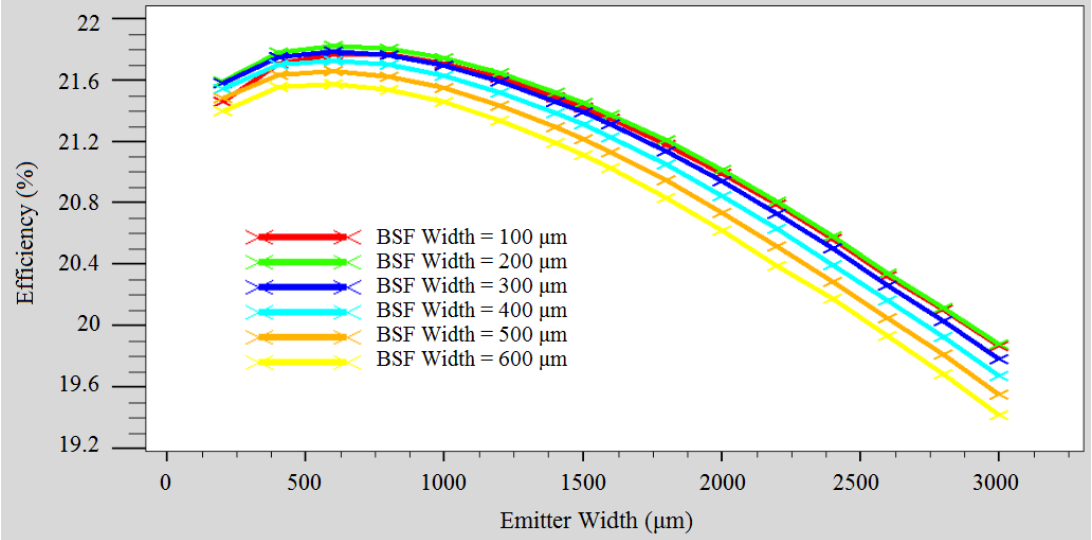

Figure 4.13: Emitter width optimization for bulk having a doping of 1x10^{15} atoms/cm^3 and lifetime of 1 ms

Another observation is that the separate lines, which stands for different BSF width values, are very close to each other without an increasing order, as it was in the high doped case. As the width of the BSF decreases the same number of carriers passes from a smaller BSF region to be collected at the contact. This density increase, results in higher amount of power loss and will be observed in BSF width sweep study much

clearly. It is also shown in chapter 4.3.4 that, the same reason plays a role for the peak efficiency formation in the emitter fraction sweep study.

In Figure 4.14 the same structure has been studied but this time with a bulk having a bulk lifetime of 10 ms. It can be observed that the peak value has shifted towards higher emitter width values when compared to Figure. The reason is, carriers, separated at the junction, will travel to BSF region much easier with a smaller recombination rate in the bulk. The bulk losses has decreased since the lifetime of a carrier in the bulk is 10 times higher than the previous case. This effect results in another observation which is the average efficiency difference of two cases. There is a noticeable increase from efficiency values around 21 to values over 23. It is an expected result since the bulk losses will be less, and greater portion of the generated carriers will be transferred to and collected at the contacts.

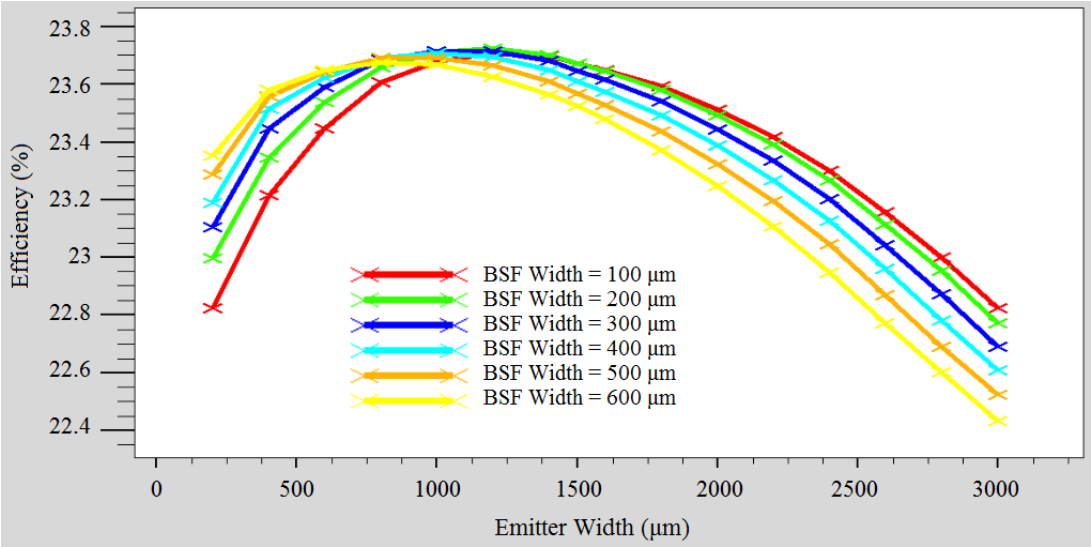

Figure 4.14: Emitter width optimization for bulk having a doping of $1x10^{15}$ and life time of 10 ms

4.3.9. BSF Width Sweep With Bulk Doping Value of $1x10^{15}$

A similar study with section 4.3.6. was performed and the results are shown in Figure, giving much clear idea about the trends for the width modifications. The BSF width sweep is performed for wider range of emitter values but with smaller average values for this case. The reason is the lower bulk doping which means a higher resistance. The increased resistance limits the carriers mobility and the optimum width values of BSF and Emitter regions shift to smaller values.

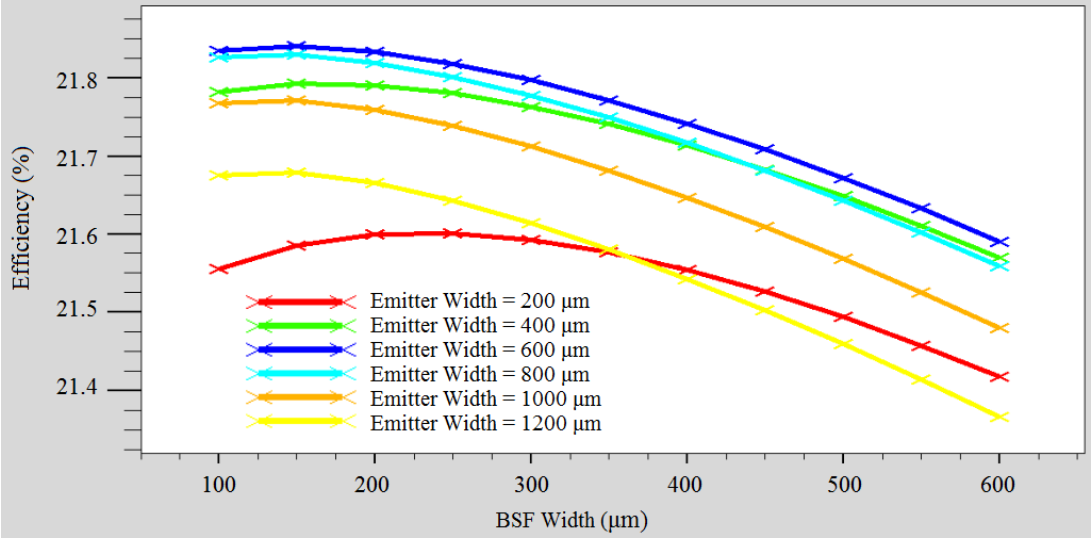

Figure 4.15: BSF width optimization for bulk having a doping of $1x10^{15}$ atoms/cm^3 and lifetime of 1 ms

The efficiency sweep is performed for Emitter width values of 200, 400, 600, 800, 1000, 1200 µm. The increasing behavior in the efficiency through decreasing BSF width can again be seen clearly with this study, however this time the efficiency starts to decrease for very small BSF width values such as 100, 150 µm. The resistive bulk causes significant resistive losses for small BSF regions.

Another observation is that for equal bulk life times, the average efficiency of the whole graph decreases when the bulk doping decreases from $1x10^{16}$ to $1x10^{15}$ atoms/cm^3 which is an expected result since the resistivity increases. However, when we increase the bulk lifetime to 10 ms, which is the realistic upper limit for bulk

doping of $1x10^{15}$ atoms/cm^3, the highest efficiency values can be reached. The results for the bulk with a life time of 10 ms can be observed in Figure 4.16.

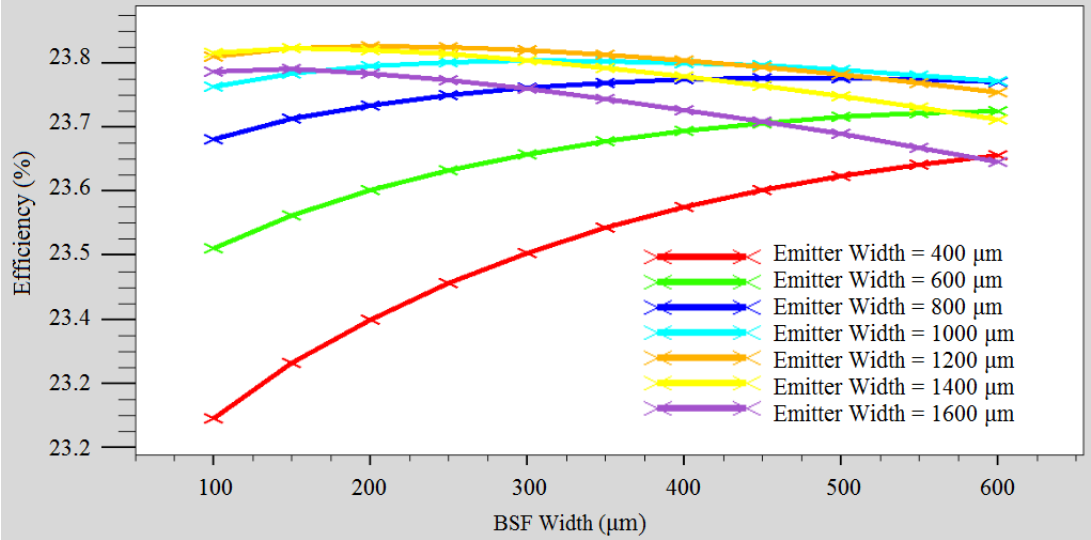

Figure 4.16: BSF width optimization for bulk having a doping of $1x10^{15}$ and life time of 10 ms

It can be easily observed that the efficiency is highest for Emitter widths of 1200, 1400 µm and BSF widths of 200, 300 µm. This result almost perfectly matches with the Emitter width sweep study given at Figure. And the balance is distrupted for sure for smaller and larger Emitter and BSF values. This conclusion is not much different than the results extracted in section 4.3.6 which gives 1500 µm wide Emitter and 300 µm wide BSF as the optimum structure. However, it shows that using a bulk with lower doping but with higher bulk lifetime gives us opportunity to reach efficiency values of almost 24%.

These results create the base of the bifacial cell study which is presented in Chapter 5. The structure used so far is a proper structure for a bifacial cell with transparent regions at non-contacted regions and the optimized Emitter, BSF width values are used as reference.

CHAPTER 5

BIFACIAL IBC CELL RESULTS

Bifacial solar cells can be categorized as a new structure when compared to traditional and IBC solar cells. Concept of bifaciality has been improved after the invention of PERT cells that includes a transparent region at the rear side of the solar cell structure. Following PERT cells, the possibility of back illumination was realized and bifacial cell trials were started. In this study, bifacial interdigitated back contacted (Bifacial IBC) solar cells were studied which is a very rare cell type and is not being studied widely. H. Ohtsuka from Central Research Laboratory has mentioned the importance of locating p-n junction to the rear side of the cell during his studies with bifacial cells[36]. The publication gives the comparison between the bifacial studies of ISFH, Sunpower, Fraunhofer ISE and Hitachi showing the advantage of Hitachi for locating p-n junction to the rear side. It is also important that the substrate used by Hitachi have a resistivity of 0.5 ohm.cm, which is smaller than the resistivity of other structures.

The main content of the study does not focus on the modular level of bifacial IBC cells, the optimizations and observations are performed at the solar cell level. The optimization of the contact widths was the main aim, considering the series resistance effect of the contacts. Series resistance effect is important for this study because both the anode and cathode contacts were placed to the rear side of the cell. These contacts should be as small as possible to allow the penetration of the light coming from the rear side. However smaller the contacts mean higher the series resistance. In this study, the tradeoff between the incoming light and increasing series resistance was studied and successful optimization was performed.

5.1. Bifaciality

Bifaciality of a bifacial solar cell is defined as the ratio of the efficiency values when the cell is illuminated from the rear side and the front side separately with an equal amount of illuminations. The ratio is smaller than 1 since the efficiency value should be smaller when the cell is illuminated from the back side.

The Fraunhofer ISE[37] had a front side efficiency of 20.6% and rear side efficiency of 19.3% where Hitachi[36] had 21.3% from the front and 19.8% from the rear side. The ratios are 0.937 for Fraunhofer ISE and 0.929 for Hitachi that are pretty high ratios with Fraunhofer leading, however, Hitachi has higher average efficiency value.

The equal amount of illuminations are given to the bifacial IBC solar cell structure studied in this thesis and the bifaciality is calculated as 83%. It means that when the structure is illuminated with the same amount of light from the rear side, 0,83 times the efficiency obtained from the normal front side illumination case is reached.

5.2. Results

The studies are performed with the same cell structure designed at the IBC study since it is also a proper bifacial IBC cell structure where it has SiNx coated transparent regions between the metal contacts at the rear side. The SiNx thickness at both sides of the structure is same since it is the optimum value for textured surfaces. For the case, the rear illumination is not included, the SiNx thickness at the rear side should be chosen differently to minimize the loss of the photons reaching the rear side, however, this portion is much smaller than 10% of the front illumination. The SiNx layer at the rear side is designed to transmit as many photons as possible to maximize the effect of rear side illumination.

The rear illumination of the structure is calculated by multiplying the front illumination profile with 0,1 0,2 0,3 values assuming the rear side illumination reaches 30% of the front side illumination at most. This value is approximated by considering

the floor reflection and geometrical limitations of installation. Then for metal coverage options of 10%, 15%, 20%, 25% and 30%, the illumination is multiplied by values of 0.9, 0.85, 0.8, 0.75 and 0.7. By this way, the shadowing effect of the metal contacts is included in the calculations. The metal resistances are not accounted during the Silvaco simulations but they are included later on by MATLAB calculations. The final optimizations are done by these modified results including the contact resistances.

The generation profile in the cell can be observed in Figure including the 30% rear illumination for a cell with a metal coverage of 10%.

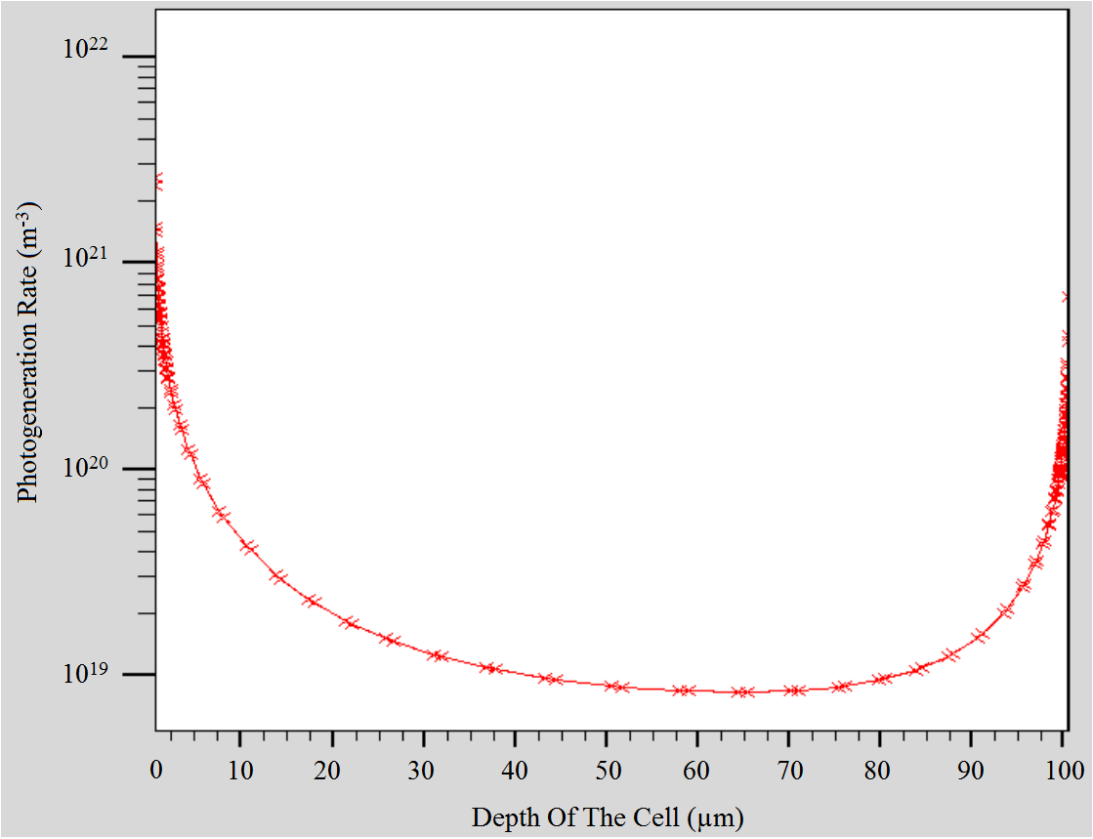

Figure 5.1: BSF width optimization for bulk having a doping of $1x10^{15}$ and lifetime of 10 ms

The two different generation profiles are merged and the electrical simulations are done with this combined generation profile. Twenty data points have been generated by Silvaco in total. Five different metal coverage values 10%, 15%, 20%,

25%, 30% are studied with four different rear side illuminations for each of them, with values of 0%, 10%, 20%, 30%. However, with Silvaco studies, the positive effect of decreasing the metal coverage couldn't be observed since the input data do not include the contact resistance values. To add contact resistances to the I-V curves of the solar cells, several modifications on the Silvaco results are performed. The I-V curves of these cells is converted into an equation with Non-Linear Curve Fitting function of Origin 8. The ideality factor "n" and the diode base current "I0" values are approximated by the following equation[12],

$$\boldsymbol{I = I_L - I_0 * \exp(\frac{V}{n * V_t})} \qquad \textbf{(Eq.64)}$$

where I is the total current and I_L is the current added by illumination, V is the voltage and V_t is the thermal voltage. After extracting the I-V curves of the cells into single diode equations, the series resistance parameter is added as follows in the MATLAB[12],

$$\boldsymbol{I = I_L - I_0 * \exp(\frac{V - I * R_S}{n * V_t})} \qquad \textbf{(Eq.65)}$$

where R_s is the series resistance value of the contacts and I * R_s is calculated as follows[12],

$$\boldsymbol{I = x * J_{mp} S_f} \qquad \textbf{(Eq.66)}$$

where S_f is the finger spacing (2mm), J_{mp} is the current density at maximum power point, and x is the distance from the end of the finger[12],

$$\boldsymbol{R_s = R_0 * \frac{dx}{w * d}} \qquad \textbf{(Eq.67)}$$

where R_0 is the effective resistivity of the metal, w is the finger width, d is the finger depth and the resistance will be calculated for element dx. Then the voltage loss V_L is calculated as follows[12],

$$\boldsymbol{V_L = I * R_s = \int S_f * J_{mp} * x \ * \ R_0 * \frac{dx}{w * d}} \qquad \textbf{(Eq.68)}$$

$$V_L = S_f * J_{mp} * \int_0^{14} x\,dx * \frac{R_0}{w * d} \qquad \textbf{(Eq.69)}$$

$$V_L = 2e-3 * \frac{14^2}{2} * \frac{1}{100e-6 * 20e-6} * J_{mp} R_0 \qquad \textbf{(Eq.70)}$$

$$V_L = 9800 * J_{mp}\left(\frac{A}{m^2}\right) * R_0(ohm * m) \qquad \textbf{(Eq.71)}$$

The effective resistivity of aluminum is approximately 3 μohm*cm however the resistivity of aluminum paste we are using in solar cell production is much higher and is given as 15 μohm*cm which is approximately 5 times higher than aluminum metal. The V_L calculation takes the following final form[12],

$$V_L = 0.000294 * J_{mp}\left(\frac{A}{m^2}\right) \qquad \textbf{(Eq.72)}$$

So the current equation can be written as follows[12],

$$I = I_L - I_0 * \exp\left(\frac{V - 0.000294 * J_{mp}\left(\frac{A}{m^2}\right)}{n * V_t}\right) \qquad \textbf{(Eq.73)}$$

Solving this equation recursively for each voltage value we end up with the final I-V curves including the contact resistance effect. Each of the 20 separate data sets produced with Silvaco is processed and new data sets are generated. In Figure the trade-off between higher light transmission and higher resistivity can be observed easily. For zero floor reflection, the increasing metal coverage increases the efficiency since the resistance will be much smaller. The fill factor also increases, following the effective collection of charges at the larger contacts.

Addition of rear illumination shows its effect with net efficiency increase. It can be observed that the red line has a higher average efficiency with respect to dark line at the bottom. Analyzing the efficiency value for constant floor reflection rate, it can be observed that a peak value around 20-25% of metal coverage can be observed. That maximum efficiency point is balanced by resistive losses at contacts and

illumination blockage by the contacts. As the the floor reflection is increased to 20%, 30% it can be observed that the peak efficiency value shifts to left side and the optimum metal coverage value shifts to 15-20%. Since the rear illumination is doubled or tripled with respect to 10% of illumination, the effect of illumination blockage is also increased and it shifts the balance to smaller contact coverage regions. Because higher illumination per area can surpass higher resistivity values and gives a new balance point with smaller contacts with higher resistivity but higher rear illumination availability at the same time.

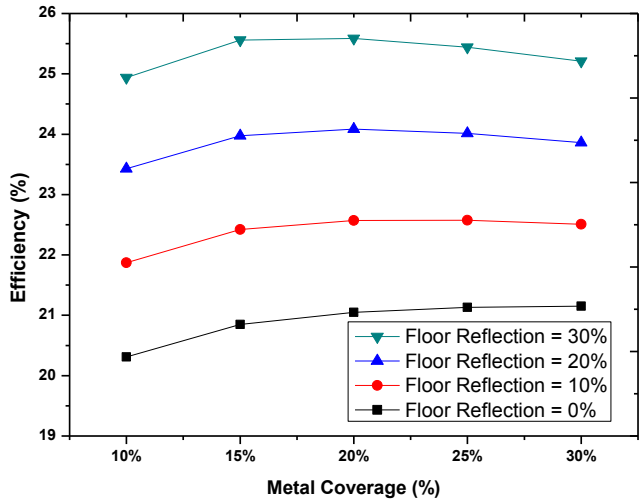

Figure 5.2: Efficiency results for Bifacial IBC cells with five different rear side metal coverages and four different floor reflection values

The study shows that, if successful floor reflectors will be used, smaller contacts should be placed to the structure at the cell level, to consolidate the amount of light penetration into the structure, by increasing the transparent area at the rear side of the cell. However, during the minimization of the contacts, the rapid increase of the series resistance should be considered and the optimum value should be studied as it is studied in this thesis.

CHAPTER 6

CONCLUSIONS

Detailed simulations, analysis and optimizations for Standard and Bifacial IBC solar cells were studied with this thesis. The OPAL 2 optical simulator was used to calculate the generation profile in the solar cell structures. Electrical simulations were performed with SILVACO TCAD tool using the exported generation profile data from the OPAL 2. Following the optimization of the IBC structure, the bifacial IBC cell rear side design and contact optimizations were also studied. The structure optimization simulations were performed for three different combinations of the bulk lifetime and doping values.

In the Bifacial IBC solar cell studies the rear side illumination was also included as an extra light source and the contacts at the rear side of the cell were optimized. The need for large contacts because of series resistance and the need for small contacts to allow rear side illumination were the main trade-off investigated in this study. To include the effect of contact resistivity, I-V curves were extracted from SILVACO TCAD and series resistance, calculated for various widths of metal fingers, were added to the one-diode equation. Efficiencies of bifacial IBC cells with various contact sizes were calculated using the generated I-V curves. A contact coverage fraction of 20% is obtained yielding the highest efficiency for a floor reflection of 30%.

REFERENCES

[1] D. D. Smith, P. Cousins, S. Westerberg, R. De Jesus-Tabajonda, G. Aniero, and Y. C. Shen, "Toward the practical limits of silicon solar cells," *IEEE J. Photovoltaics*, vol. 4, no. 6, pp. 1465–1469, 2014.

[2] K. (2017). Yoshikawa, Kunta & Yoshida, Wataru & Irie, Toru & Kawasaki, Hayato & Konishi, Katsunori & Ishibashi, Hirotaka & Asatani, Tsuyoshi & Adachi, Daisuke & Kanematsu, Masanori & Uzu, Hisashi & Yamamoto, "Exceeding conversion efficiency of 26% by h."

[3] J. Nelson, "The Phisics of Solar Cells," *Prop. Semicond. Mater.*, p. 384, 2003.

[4] NREL, "Silicon Materials and Devices R&D." [Online]. Available: http://www.nrel.gov/pv/silicon_materials_devices.html.

[5] A. Back *et al.*, "20 . 1 % Efficient Silicon Solar Cell With," vol. 32, no. 8, pp. 1101–1103, 2011.

[6] J. Zhao, A. Wang, and M. a. Green, "24·5% Efficiency silicon PERT cells on MCZ substrates and 24·7% efficiency PERL cells on FZ substrates," *Prog. Photovoltaics Res. Appl.*, vol. 7, no. August, pp. 471–474, 1999.

[7] M. Taguchi *et al.*, "24.7% Record efficiency HIT solar cell on thin silicon wafer," *IEEE J. Photovoltaics*, vol. 4, no. 1, pp. 96–99, 2014.

[8] Panasonic Corporation, "Panasonic HIT® Solar Cell Achieves World's Highest Energy Conversion Efficiency*1 of 25.6%*2 at Research Level."

[9] I. Repins *et al.*, "Characterization of 19.9%-efficient CIGS absorbers," *Conf. Rec. IEEE Photovolt. Spec. Conf.*, 2008.

[10] X. Wu, “High-efficiency polycrystalline CdTe thin-film solar cells,” *Sol. Energy*, vol. 77, no. 6, pp. 803–814, 2004.

[11] C. B. Honsberg and A. M. Barnett, “Paths to Ultra-High Efficiency (>50% Efficient) Photovoltaic Devices,” *20th Eur. Photovolt. Sol. Energy Conf.*, no. June, pp. 453–456, 2005.

[12] W. Nie *et al.*, “High-efficiency solution-processed perovskite solar cells with millimeter-scale grains,” *Science (80-.).*, vol. 347, no. 6221, pp. 522–525, 2015.

[13] M. a. Green, “Solar Cells: Operating Principle.” p. 2, 1982.

[14] T. O. M. Tiedje, E. L. I. Yablonovitch, G. D. G. D. Cody, and B. G. B. G. B. G. Brooks, “Limiting Efficiency of Silicon,” *IEEE Trans. Electron Devices*, vol. 31, no. 5, pp. 711–716, 1984.

[15] S. Gatz, T. Dullweber, and R. Brendel, “Evaluation of series resistance losses in screen-printed solar cells with local rear contacts,” *IEEE J. Photovoltaics*, vol. 1, no. 1, pp. 37–42, 2011.

[16] N. J. Ekins-Daukes *et al.*, “Controlling radiative loss in quantum well solar cells,” *J. Phys. D. Appl. Phys.*, vol. 46, no. 26, p. 264007, 2013.

[17] R. De Rose, P. Magnone, M. Zanuccoli, E. Sangiorgi, and C. Fiegna, “Loss analysis of silicon solar cells by means of numerical device simulation,” *2013 14th Int. Conf. Ultim. Integr. Silicon*, pp. 205–208, 2013.

[18] Z. Yu, A. Raman, and S. Fan, “Fundamental limit of nanophotonic light trapping in solar cells.,” *Proc. Natl. Acad. Sci. U. S. A.*, vol. 107, no. 41, pp. 17491–6, 2010.

[19] A. G. Aberle, “Surface passivation of crystalline silicon solar cells: a review,” *Prog. Photovoltaics Res. Appl.*, vol. 8, no. 5, pp. 473–487, 2000.

[20] M. I. B.L. Sopori, R.A. Pryor, “Design of antireflection coatings for textured silicon solar cells,” 2003.

[21] D. Chandler-Horowitz and P. M. Amirtharaj, “High-accuracy, midinfrared (450 cm[sup −1]≤ω≤4000 cm[sup −1]) refractive index values of silicon,” *J. Appl. Phys.*, vol. 97, no. 2005, p. 123526, 2005.

[22] A. Blakers, “Shading losses of solar-cell metal grids,” *IEEE Xplore*, 1992.

[23] P. Taylor, A. I. Lvovsky, and A. I. Lvovsky, “Fresnel Equations,” *Encycl. Opt. Eng.*, no. August, pp. 37–41, 2013.

[24] K. R. McIntosh and S. C. Baker-Finch, “OPAL 2: Rapid optical simulation of silicon solar cells,” *Conf. Rec. IEEE Photovolt. Spec. Conf.*, pp. 265–271, 2012.

[25] S. C. Baker-Finch and K. R. McIntosh, “A freeware program for precise optical analysis of the front surface of a solar cell,” *Conf. Rec. IEEE Photovolt. Spec. Conf.*, no. July 2010, pp. 2184–2187, 2010.

[26] M. A. Green, “Lambertian light trapping in textured solar cells and light-emitting diodes: Analytical solutions,” *Prog. Photovoltaics Res. Appl.*, vol. 10, no. 4, pp. 235–241, 2002.

[27] W. Tobocman and C. Western, “• r ’) n â€TM ß V â€TM G (r , r ’) = • r), r • M , (la) T (k) • k • dS,” 1984.

[28] D. S. Software, “Atlas User ’ s Manual,” no. 408, pp. 567–1000, 2014.

[29] A. Richter, S. W. Glunz, F. Werner, J. Schmidt, and A. Cuevas, “Improved quantitative description of Auger recombination in crystalline silicon,” *Phys. Rev. B - Condens. Matter Mater. Phys.*, vol. 86, no. 16, pp. 1–14, 2012.

[30] B. Van Zeghbroeck, “Principles of Semiconductor Devices,” 2011. [Online]. Available: http://ecee.colorado.edu/~bart/book/book/chapter2/ch2_8.htm. [Accessed: 25-Oct-2016].

[31] S. Clara, “User’s Manual,” no. 408, pp. 567–1000, 2007.

[32] A. Fell *et al.*, “Input parameters for the simulation of silicon solar cells in 2014,” *IEEE J. Photovoltaics*, vol. 5, no. 4, pp. 1250–1263, 2015.

[33] C. Gong *et al.*, “Screen-Printed Aluminum-Alloyed P + Emitter on Back-Contact Silicon Solar Cells,” vol. 31, no. 6, pp. 576–578, 2010.

[34] R. Woehl, J. Krause, F. Granek, and D. Biro, “Back-Junction Silicon Solar Cell With Aluminum-Alloyed Emitter,” *Sol. Energy*, vol. 32, no. 3, pp. 345–347, 2011.

[35] L. J. Koduvelikulathu *et al.*, “2-D Modeling of n-Type IBC Solar Cells Using SILVACO ATLAS Simulation,” *Nusod 2011*, pp. 3–4, 2011.

[36] Y. Ohtsuka, H, Sakamoto, M, Tsutsui, K, Yazawa, J. Wiley, S. Energy, and S. P. Corp, “Bifacial Silicon Solar Cells with 10=2) Front Ef_ciency and 08=7) Rear Ef_ciency,” *Qual. Assur.*, no. June, pp. 274–279, 1999.

[37] S. W. Glunz, “Optimized high-efficiency silicon solar cells,” no. June 2017, pp. 2–6, 1997.

[38] M. A. Maehlum, “Best Thin Film Solar Panels – Amorphous, Cadmium Telluride or CIGS?,” 2015.

[39] P. V. M. Andreev, “GaInP/GaAs tandem cells,” *Sol. Cells*.

[40] D. H. P.S.Priambodo, N.R. Poespawati, “Chapter book: Solar Cell Technology, Fitting The I-V Curve.”

[41] “Theory of Solar Cells.” [Online]. Available: https://en.wikipedia.org/wiki/Theory_of_solar_cells. [Accessed: 21-Dec-2016].

[42] electrical4u, “p-n Junction Diode and Characteristics of p-n Junction.” [Online]. Available: http://www.electrical4u.com/p-n-junction-diode/. [Accessed: 20-Jan-2017].

APPENDIX A

Silvaco Code for setting the structure (Starts with "GO ATHENA") and for performing the electrical simulation (Starts with "GO ATLAS"):

```
GO ATHENA
LINE X      LOCATION=<VALUE>     SPACING=<VALUES>
LINE Y      LOCATION=<VALUE>     SPACING=<VALUES>
LINE X      LOCATION =0.00                      SPACING=10
LINE X      LOCATION =$wbase/2                  SPACING=5
LINE X      LOCATION =$wbase/2+$wgap            SPACING =5
LINE X      LOCATION =$wcell/2-$wemit/4         SPACING =40
LINE X      LOCATION =$wcell/2-20               SPACING =5
LINE X      LOCATION =$wcell/2+20               SPACING =5
LINE X      LOCATION =$wcell/2+$wemit/4         SPACING =40
LINE X      LOCATION =$wcell-$wbase/2-$wgap     SPACING =5
LINE X      LOCATION =$wcell-$wbase/2           SPACING =5
LINE X      LOCATION =$wcell                    SPACING =10
SET    wemit = 1500
SET    wgap  = 100
SET    wbase = 300
SET    wcell = $wemit+2*$wgap+$wbase
SET    depth = 200
LINE Y      LOCATION=0.00                       SPACING =0.05
LINE Y      LOCATION=1                          SPACING =0.1
LINE Y      LOCATION=10                         SPACING =10
LINE Y      LOCATION=100                        SPACING =10
LINE Y      LOCATION=$depth-10                  SPACING =10
```

```
LINE Y        LOCATION=$depth-1                    SPACING =0.04
LINE Y        LOCATION=$depth                      SPACING =0.04

INIT SILICON          C.PHOS=1e15        ORIENTATION=100 TWO.D
DEPOSIT OXIDE         THICKNESS=0.5      DIVISION=4
ETCH OXIDE RIGHT      P1.X=$wbase/2+2*$wgap+$wemit
ETCH OXIDE LEFT       P1.X=$wbase/2
DIFFUSE       TIME=1 hour  TEMPRATURE=1000   C.PHOS = $dopingbsf
ETCH OXIDE
DEPOSIT ALUMINUM      THICKNESS =0.1     DIVISION=4

ETCH ALUMINUM START       X=$metal/2                   Y=-$depth-10
ETCH CONT         X=$metal/2                           Y=-$depth
ETCH CONT         X =$wbase/2+$wgap+$wemit/2-$metal/2  Y=-$depth
ETCH DONE         X =$wbase/2+$wgap+$wemit/2-$metal/2  Y=-$depth-10

ETCH ALUMINUM START   X =$wbase/2+$wgap+$wemit/2+$metal/2   Y=-
$depth-10
ETCH CONT         X =$wbase/2+$wgap+$wemit/2+$metal/2  Y=-$depth
ETCH CONT         X =$wcell-$metal/2                   Y=-$depth
ETCH DONE         X =$wcell-$metal/2                   Y=-$depth-10

ELECTRODE         NAME=BSF          X=25
ELECTRODE         NAME =BSF         X=$wcell-25
ELECTRODE         NAME =emitter     X=$wbase/2+$wgap+$wemit/2
STRUCTURE         OUTF=IBC01_0.str
```

```
GO ATLAS
MATERIAL    MATERIAL=Silicon TAUN0=1e-3  TAUP0=1e-3

CONTACT     NAME=emitter   SURF.REC VSURFN=10000000
VSURFP=10000000

CONTACT     NAME =base      SURF.REC VSURFN=10000000
VSURFP=10000000

INTERFACE     X.MIN=0     X.MAX=20000          Y.MIN=-5       Y.MAX =5
S.N =5000 S.P=5000   S.I

INTERFACE     X.MIN=0     X.MAX=$wbase/2       Y.MIN=80     Y.MAX =300
S.N =5000 S.P=5000   S.I

INTERFACE     X.MIN =$wbase/2+$wgap  X.MAX =$wbase/2+$wgap+$wemit
Y.MIN =80      Y.MAX =300             S.N =5000 S.P=5000  S.I

INTERFACE     X.MIN =$wcell-$wbase/2   X.MAX =$wcell          Y.MIN =80
Y.MAX =300   S.N =5000 S.P=5000  S.I

INTERFACE     X.MIN =$wbase/2              X.MAX =$wbase/2+$wgap Y.MIN
=80       Y.MAX =300            S.N =30 S.P=30         S.I

INTERFACE     X.MIN=$wbase/2+$wgap+$wemit X.MAX=$wbase/2+$wgap+
$wemit+$wgap          Y.MIN =80  Y.MAX =300  S.N=30 S.P=30   S.I

DATASET       INFILE=200UmgentextureWRT.log          NAME=photo
ABS.CHAR      AXIS.YXZ     FY1=0 FY2=200 TY1=0 TY2=200

BEAM  NUMBER=1 CHARACTER=photo

LOG outfile=IBC01_01.log

SOLVE          INIT

SOLVE          B1=1.0
```

```
SOLVE NAME=emitter VBASE=0.0 VSTEP=0.02 VFINAL=0.76

STRUCTURE OUTF=IBC01_02.str

TONYPLOT IBC01_01.log

TONYPLOT IBC01_02.str


SOLAR IV="Voc,Jsc,Pmax,FF”

EXTRACT INIT INFILE="IBC01_01.log"

EXTRACT NAME="Jsc" Y.VAL FROM CURVE(v."emitter", i."base") WHERE X.VAL =0.001

EXTRACT NAME ="P" CURVE(v."emitter", (v."emitter" * i."base")) OUTF="solarex12_P.dat"

EXTRACT NAME="Pm"MAX(CURVE(v."emitter",(v."emitter" *i."base")))

EXTRACT NAME ="Vm" X.VAL FROM CURVE(v."emitter", (v."emitter" * i."base") ) WHERE Y.VAL =$"Pm"

EXTRACT NAME ="Im" $"Pm"/$"Vm"

EXTRACT NAME ="JscmAcm2" $Jsc*1e08*1e03/$wcell

EXTRACT NAME ="Voc" X.VAL FROM CURVE(v."emitter", i."base") WHERE Y.VAL=0.0

EXTRACT NAME ="FF" $"Pm"/($"Jsc"*$"Voc")*100

EXTRACT NAME ="Eff" ($Pm*1e08/(0.100037*$wcell))*100

EXTRACT NAME ="IV" CURVE(v."emitter", i."base")
 OUTF="STRUCTURE OUTF=IBC01_02.dat"
```

APPENDIX B

Matlab Code for adding the series contact resistance effect to the I-V curve extracted from Silvaco:

```
IL= %Calculated with Non-Linear Fit function of Origin 8
I0= %Calculated with Non-Linear Fit function of Origin 8
n=  %Calculated with Non-Linear Fit function of Origin 8
k=0.8
b=1
c=zeros(100*k+1,1)

for a2=0:1:6
   b=1
for a=0:0.01:k
   c(b,1) =IVfunc(a,n,c(b,1),I0,IL)
   b=b+1
end
end

figure, plot(0:0.01:k,c)
axis([0 k -5 55])
xlabel('Voltage'), ylabel('Jsc')
title('I-V Curve')

b=1
t=zeros(100*k+1,1)
for a=0:0.01:0.62
   t(b,1) =c(b,1)*a
   b=b+1
end
[m1,m2]= max(t)
JMP = c(m2,1)
Voc = 18.67*0.02586*n
```

Current calculation function used in the previous code.

```
function [ I ] = IVfunc( v,n,Js,I0,IL )
% 0.000294 for Ro=3Uohm.cm
I= IL-(I0*(exp((v+0.00294*Js)/(0.02586*n))-1))
end
```